*Article*

# Comparative Study of CoFe$_2$O$_4$ Nanoparticles and CoFe$_2$O$_4$-Chitosan Composite for Congo Red and Methyl Orange Removal by Adsorption

**Claudia Maria Simonescu** [1,*] ⓘ, **Alina Tătăruş** [1,2] ⓘ, **Daniela Cristina Culiţă** [3,*] ⓘ, **Nicolae Stănică** [3], **Ioana Alexandra Ionescu** [2], **Bogdan Butoi** [4] ⓘ **and Ana-Maria Banici** [4]

1. Department of Analytical Chemistry and Environmental Engineering, Faculty of Applied Chemistry and Materials Science, Politehnica University of Bucharest, Polizu Street, No. 1-7, District 1, 011061 Bucharest, Romania; alina.tatarus@yahoo.com
2. National Research and Development Institute for Industrial Ecology, INCD ECOIND Bucuresti, 71-73 Drumul Podul Dambovitei Str., 060652 Bucharest, Romania; ioana.ionescu@incdecoind.ro
3. Ilie Murgulescu Institute of Physical Chemistry, 202 Splaiul Independentei, 060021 Bucharest, Romania; nstanica@icf.ro
4. National Institute for Laser, Plasma and Radiation Physics, 077125 Măgurele, Romania; bogdan.butoi@inflpr.ro (B.B.); niculescu.anam@gmail.com (A.-M.B.)
*   Correspondence: claudiamaria_simonescu@yahoo.com or claudia.simonescu@upb.ro (C.M.S.); danaculita@yahoo.co.uk (D.C.C.); Tel.: +40-753071418 (C.M.S.); +40-765309363 (D.C.C.)

**Abstract:** (1) Background: A comparative research study to remove Congo Red (CR) and Methyl Orange (MO) from single and binary solutions by adsorption onto cobalt ferrite (CoFe$_2$O$_4$) and cobalt ferrite–chitosan composite (CoFe$_2$O$_4$-Chit) prepared by a simple coprecipitation method has been performed. (2) Methods: Structural, textural, morphology, and magnetic properties of the obtained magnetic materials were examined by X-ray diffraction (XRD), Fourier-transform infrared (FTIR) spectroscopy, N$_2$ adsorption–desorption analysis, Scanning Electron Microscopy (SEM), Transmission Electron Microscopy (TEM), and magnetic measurements. The optimal operating conditions of the CR and MO removal processes were established in batch experiments. The mathematical models used to describe the processes at equilibrium were Freundlich and Langmuir adsorption isotherms. (3) Results: Cobalt ferrite–chitosan composite has a lower specific surface area ($S_{BET}$) and consequently a lower adsorption capacity than cobalt ferrite. CoFe$_2$O$_4$ and CoFe$_2$O$_4$–Chit particles exhibited a superparamagnetic behavior which enabled their efficient magnetic separation after the adsorption process. The research indicates that CR and MO adsorption onto prepared magnetic materials takes place as monolayer onto a homogeneous surface. According to Langmuir isotherm model that best fits the experimental data, the maximum CR/MO adsorption capacity is 162.68/94.46 mg/g for CoFe$_2$O$_4$ and 15.60/66.18 mg/g for CoFe$_2$O$_4$–Chit in single solutions. The results of the kinetics study revealed that in single-component solutions, both pseudo-first-order and pseudo-second-order kinetics models represent well the adsorption process of CR/MO on both magnetic adsorbents. In binary solutions, adsorption of CR/MO on CoFe$_2$O$_4$ better follows the pseudo-second-order kinetics model, while the kinetic of CR/MO adsorption on CoFe$_2$O$_4$–Chit is similar to that of the dyes in single-component solutions. Acetone and ethanol were successfully used as desorbing agents. (4) Conclusions: Our study revealed that CoFe$_2$O$_4$ and CoFe$_2$O$_4$–Chit particles are good candidates for dye-contaminated wastewater remediation.

## 1. Introduction

Improper disposal of pollutants such as heavy metal ions, dyes, pharmaceutical wastes, pesticides, organic compounds into aquatic environments constitutes one of the

significant environmental issues that is facing the entire world [1]. Dyes are basic chemical compounds that are utilized in many industrial practices such as textile, paper, leather, plastics and rubber, food, pharmaceutical, and cosmetics industrial practices. At the industrial level, more than 10,000 dyes and pigments are used in various fields [2]. Dyes are intensely colored substances that present special problems in wastewater, even in very small quantities. However, the effect is more unpleasant from an aesthetic point of view, rather than dangerous, for example, red dyes spilled into rivers and oceans.

Dye molecules are mutagenic, carcinogenic, and cause dysfunction in the following organs: the kidneys, liver, brain, and reproductive and central nervous system [2]. When effluents with dyes are discharged into various water sources, the turbidity of the water increases as the effluents will produce a visible layer on the surface of the water sources due to the low density ($0.8 \, kg/m^3$) compared to the density of water ($1 \, kg/m^3$) [3]. The sunlight necessary for the processes of photosynthesis and respiration of aquatic organisms will not penetrate through the dye layer determining the death or aquatic organisms. The decrease in soil productivity can be registered in the situation when effluents containing dyes will be discharged in soils by blocking their pores [3].

Dyes used in the textile industry have negative effects on the DNA in cells, raising the risk of cancer. Those used in the food industry are associated with the appearance of hives, allergies, asthma, hyperactivity, irritability, aggression, dermatitis, and angioedema [4], and those used in the pharmaceutical industry are known to cause skin irritations. Bladder, blood and bone marrow cancer, fertility problems, and allergies can be caused by dyes in the cosmetics industry [4]. Cationic and anionic dyes are toxic due to the aromatic cycle present in their structure. The degradation of dyes is not easy and can induce the following diseases: dizziness, jaundice, cyanosis, burns, allergic problems, vomiting, diarrhea, nausea, and even effects on development and mental health [4].

Thus, it is essential to remediate waters and wastewater containing dyes using environmentally friendly, cost-effective, and efficient treatment methods. Among all the approaches for the depollution of dye-contaminated waters, comprising chemical methods (coagulation, flocculation, oxidation, etc.), physical (filtration, adsorption, irradiation, ion exchange, membrane processes, etc.), and biological approaches (microbial discoloration), adsorption is the most commonly used process owing to the simplicity and wide variety of existing natural and man-made adsorbent materials.

Numerous types of materials such as activated carbon [5], zeolites [6], lignocellulosic materials [7], clays [8], double-layered hydroxides [9], metal-organic networks (MOFs) [10], magnetic materials [11], metal oxides [12], graphene oxide [13], silica [14], polymeric materials [15,16], carbon nanotubes [17], agricultural wastes [18], chitosan [19], food-processing by-products [20], clays [21], dendritic polymers [22], and hydroxyapatite based materials [23] were applied as dye adsorbents in synthetic aqueous solutions and industrial wastewater.

The disadvantages, such as the high cost of adsorbents and the difficulties of separation after the wastewater treatment process, do not promote their widespread use. The separation of pollutant-loaded adsorbents can be performed by centrifugation, free settling, and membrane filtration. These separation methods involve complicated technical equipment and high operational and maintenance costs. Therefore, they have to be replaced by other efficient methods in water/wastewater treatment applications. One of the most important and economically efficient separation methods is magnetic separation [23–28]. This can be applied instead of filtration and centrifugation. Thus, it is necessary to develop and test new magnetic materials to remove dyes from wastewater because they are important in this field having high adsorption capacity and magnetic properties that are important in removing pollutants from water/wastewater. Hence, cobalt ferrite ($CoFe_2O_4$) and cobalt ferrite–chitosan composite ($CoFe_2O_4$-Chit) have been prepared by a simple coprecipitation method. The main advantages of preparing cobalt ferrite–chitosan composite are that the obtained microparticles can be applied in batch and column systems, as compared to cobalt ferrite nanoparticles that are suitable to be used only in batch systems, and they

can be easily removed from treated water using an external magnetic field. The optimum experimental conditions of the Congo Red and Methyl Orange removal onto magnetic materials were established in batch systems from single and binary solutions. The isothermal and kinetic study was accomplished to emphasize the Congo Red and Methyl Orange removal mechanisms. Desorption tests have been applied to prove the reusability of the materials tested.

## 2. Materials and Methods

### 2.1. Materials

Fe(NO$_3$)$_3$·9H$_2$O 96%, Co(NO$_3$)$_2$·6H$_2$O, chitosan, and glacial acetic acid (analytical grade, Sigma-Aldrich Chemie GmbH, Steinheim, Germany) were used in the synthesis of magnetic materials. NaOH pellets, HCl 35% suprapure and NH$_4$OH 25% (analytical grade) were purchased from Merck KGaA Darmstadt, Germany. Congo Red (CR) 99% (C$_{32}$H$_{22}$N$_6$Na$_2$O$_6$S$_2$) and Methyl Orange (MO) (ACS reagent, dye content 85 %, C$_{14}$H$_{14}$N$_3$NaO$_3$S, Sigma-Aldrich Chemie GmbH, Steinheim, Germany) and ultrapure water were used for preparing the dye solutions. Ethyl alcohol (95%) and acetone (99%) (Sigma-Aldrich Chemie GmbH, Steinheim, Germany) were used as desorbing agents, while ammonium acetate 99% and acetonitrile 99% (Merck KGaA Darmstadt, Germany) as mobile phase for chromatographic separation and detection were used.

### 2.2. Characterization Methods and Instruments

The magnetic materials were characterized by analytical techniques such as Fourier-transform infrared (FTIR) analysis, N$_2$ sorption analysis, X-ray diffraction, SEM/TEM, and magnetic measurements. FTIR spectra (4000–400 cm$^{-1}$) were registered on a JASCO FT/IR-4700 spectrometer (Tokyo, Japan) using KBr pellets. The specific surface areas (S$_{BET}$) of the magnetic materials were analyzed by N$_2$ adsorption–desorption at −196 °C using a Micromeritics ASAP 2020 automatic adsorption system (Norcross, GA, USA). The Brunauer–Emmett–Teller method on the partial pressure adsorption data (P/Po) in the range 0.05–0.3 was involved in determination of S$_{BET}$ values. XRD structural characterization was performed with a Panalytical X'Pert Pro MPD equipment (Malvern, Worcestershire, UK) in Bragg–Brentano configuration, continuous scanning in the range 5°−85° deg 2θ, with a step of 0.02° and an acquisition time varying from 15 s/step to 45 kV and 40 mA to 30 s/step in order to increase the resolution in the case of the CoFe$_2$O$_4$–Chit sample. A divergent slit was used on the incident beam, and a nickel filter and a curved graphite monochromator were placed on the diffracted beam, obtaining a monochromatic CuKα radiation of λ = 0.15418 nm. Calculations of the average crystallite size and identification of crystalline phases were performed using Panalytical's HighScore Plus software and the ICDD (International Center of Diffraction Data) database. SEM images of magnetic materials have been recorded on QUANTA FEG-250 (FEI producer, Brno, Czech Republic) type instrument. For microstructural investigations, the JEOL 2100 Transmission Electron Microscope (TEM) equipped with JEOL Energy Dispersive Spectroscopy (EDS) Detector (Akishima, Tokyo, Japan) has been used. The TEM specimen has been prepared using the standard powder method, using a Cu grid. The magnetic properties were measured at room temperature on Lake Shore's fully integrated Vibrating Sample Magnetometer system 7404 (VSM) (Westerville, OH, USA).

The performance of magnetic materials in CR and MO removal process has been explored in batch tests performed on GFL 3015 orbital shaker (Burgwedel, Germany) at 150 rpm (rotation per minute). An Agilent 3200 laboratory pH-meter (Agilent Technologies, Shanghai, China) was utilized to evaluate the dye solution's pH.

The chromatographic separation and detection were performed on an Agilent 1200 series HPLC (Tokyo, Japan) in order to determine the CR and MO concentration in initial solutions and after the removal process. The system has a semipermeable membrane degasser, quaternary pump, self-sampler with variable injection volume (0.1–100 μL), thermostatted column compartment, and a Diode Array Detector (DAD) with the capacity to

register simultaneously UV-Vis spectra (190–900 nm) and up to 8 discrete wavelengths. Data acquisition, processing, and reporting has been accomplished with Agilent Chem-Station software. The mobile phase was 30% aqueous phase (100 mM ammonium acetate, pH 5) and 70% organic solvent (Acetonitrile) (*v/v*), which resulted in a narrow and high symmetry Congo Red peak. All chromatographic runs were carried out on an Acclaim Surfactant Plus column (150 × 3.0 mm, 3.0 μm) from Thermo Scientific. The injection volume was 10 μL and column was kept at 30 °C. The chromatogram run-time was only 12 min (Methyl Orange retention time approx. 6 min and Congo Red retention time approx. 12 min) (Figure 1). Detection of the Congo Red and Methyl Orange compounds was carried out at the optimal wavelengths identified after the maximum absorption in UV-Vis severs: λ = 506 nm (Congo Red) and λ = 428 nm (Methyl Orange). Figures S1 and S2 show the UV-Vis absorption spectra of Congo Red obtained by High-Performance Liquid Chromatography with Diode-Array Detector (HPLC-DAD) method.
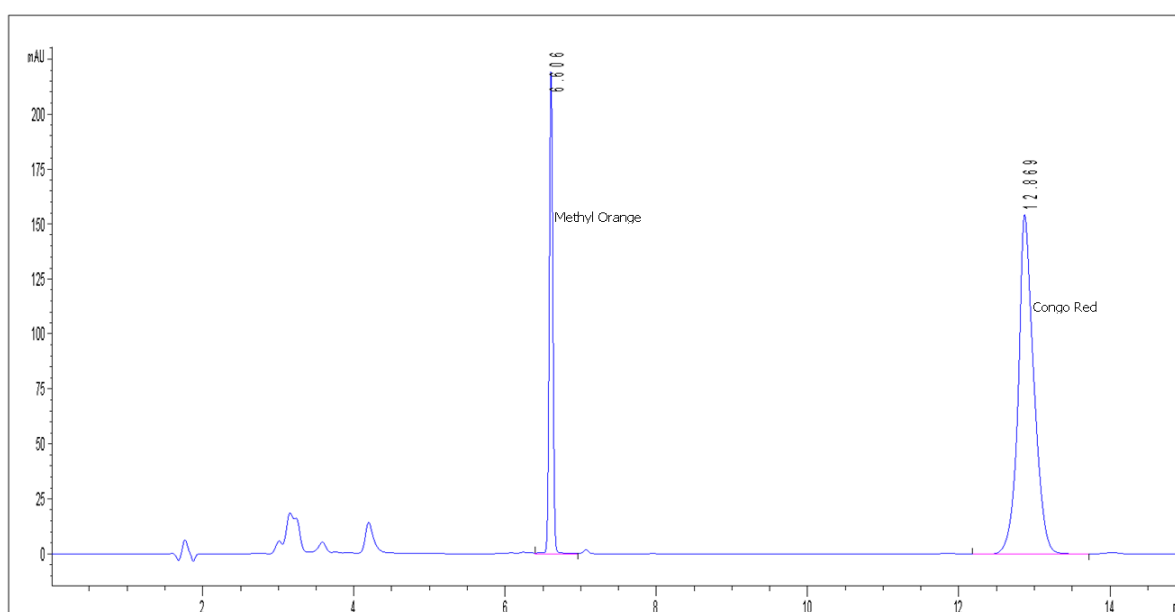


**Figure 1.** Chromatogram obtained from the analysis of Congo Red (CR) and Methyl Orange (MO).

Method calibration curves were obtained using Congo Red and Methyl Orange aqueous solutions of: 0.1, 0.2, 0.5, 1, 2.5, 5, and 10 mg/L (Figures S3 and S4).

### 2.3. The Adsorbents Synthesis Protocol

Fe(NO$_3$)$_3$·9H$_2$O 96% and Co(NO$_3$)$_2$.6H$_2$O were used as source of Fe(III) and Co(II) ions, respectively, for cobalt ferrite (CoFe$_2$O$_4$) synthesis. To an aqueous solution containing Fe(NO$_3$)$_3$·9H$_2$O and Co(NO$_3$)$_2$.6H$_2$O in molar ratio (2:1), 60 mL of NH$_4$OH 25% solution was added to precipitate the cobalt ferrite. The obtained mixture was heated at 80 °C, under stirring for 3 h. The resulting precipitate was filtered and washed several times with distilled water.

For the synthesis of cobalt ferrite–chitosan composite (CoFe$_2$O$_4$-Chit), cobalt ferrite nanoparticles synthesized as described above were added to a chitosan gel prepared by dissolving 0.25 g of chitosan in 25 mL of 10% acetic acid. The cobalt ferrite suspension in chitosan was stirred for 1 h (room temperature and 500 rpm) then dropped with a syringe into 500 mL 30% NaOH. CoFe$_2$O$_4$-Chit particles were stirred for 14 h (at room temperature and 500 rpm) to complete the chitosan precipitation process on the cobalt ferrite surface. Upon completion of the coating process, CoFe$_2$O$_4$–Chit particles were washed with ultrapure water and dried in an oven at 60 °C for 3 h.

*2.4. The Adsorption and Desorption Protocol*

To study the influence of operational parameters on the adsorption capacity of $CoFe_2O_4$ and $CoFe_2O_4$–Chit, batch tests were performed in the following experimental conditions:

(i) A total of 25 mL dye solution in contact with 0.01 g $CoFe_2O_4$/$CoFe_2O_4$–Chit at room temperature;

(ii) A pH range of 2.22–10.8; HCl and $NH_4OH$ solutions of various concentrations have been used for changing the pH of the dye solution;

(iii) Contact time between 5 and 360 min;

(iv) Initial dye concentration ranged from 4.98 to 102.81 mg/L;

(v) Single CR/MO and binary CR + MO solutions were investigated;

(vi) Five recyclability experiments were performed by the use of 25 mL of desorbing agent and 0.01 g magnetic materials loaded with dye, for 4 h contact time at 150 rpm and at room temperature.

After adsorption, the adsorbent was removed from solution using a hand-held neodymium magnet, and the residual concentration of dye was determined.

The amount of dye retained per gram of $CoFe_2O_4$/$CoFe_2O_4$–Chit at equilibrium and at various contact times was estimated using the Equation (1):

$$Q_t = \frac{(C_0 - C_t) \times V}{m} \tag{1}$$

where $Q_t$—represents the removal/adsorption capacity which is the amount of CR/MO retained per gram of $CoFe_2O_4$/$CoFe_2O_4$–Chit at various contact times (mg/g);

$C_0$—the CR/MO initial concentration (mg/L);

$C_t$—the CR/MO concentration at time ($t$) of contact with adsorbent (or at different pH values) (mg/L);

$V$—the dye solution volume (L);

$m$—the amount of $CoFe_2O_4$/$CoFe_2O_4$-Chit used as adsorbent (g).

The desorption efficiency has been calculated by the use of Equation (2) [29]:

$$D(\%) = \left( \frac{Q_D}{Q_e} \right) \times 100 \tag{2}$$

where $Q_D$ is desorption capacity calculated with Equation (3) (mg/g).

$Q_e$ means the adsorption capacity at equilibrium (mg/g):

$$Q_D = \frac{C_f}{m} \times V \tag{3}$$

where $C_f$ constitutes final concentration of CR/MO desorbed (in solution) (mg/L);

$V$ is the eluent volume (L);

$m$ represents the amount of $CoFe_2O_4$/$CoFe_2O_4$–Chit loaded with dye (g).

All the experiments have been performed in triplicate and the maximum experimental error is 5%.

*2.5. The Mathematical Modeling of Adsorption Process*

Understanding the adsorbent–adsorbate relationship, the distribution of adsorbed molecules at equilibrium between the solid and liquid systems through the sorption isotherms is useful for explaining the processes of adsorption of pollutants. In addition, the adsorption capacity of adsorbents can be predicted using mathematical modeling of the adsorption process by means of adsorption isotherms. The most used adsorption isotherm models for this purpose are Langmuir and Freundlich isotherms. These isotherms are expressed in the form of the following mathematical equations:

(i) Nonlinear form of the Langmuir isotherm equation [30]:

$$Q_e = \frac{Q_{max}K_L C_e}{1 + K_L C_e} \qquad (4)$$

where $C_e$ constitutes CR/MO concentration at equilibrium (in solution) (mg/L);

$K_L$ is the equilibrium constant of the Langmuir model connected with the adsorption energy (L/mg);

$Q_e$ means the adsorption capacity at equilibrium (mg/g);

$Q_{max}$ is the maximum adsorption capacity (mg/g).

(ii)   Nonlinear for the Freundlich isotherm equation [31]:

$$Q_e = K_F \times C_e^{\frac{1}{n}} \qquad (5)$$

where $K_f$ (mg/g) is adsorption capacity determined from Freundlich equation;

$1/n$ represents Freundlich parameter with respect to adsorption intensity;

$C_e$ is CR/MO concentration at equilibrium (in solution) (mg/L).

The kinetics of the CR retention process on prepared magnetic materials have been studied for their possible transformation from laboratory-scale experiments to pilot-scale remediation of industrial wastewater containing dyes. Therefore, the kinetic description of CR/MO remediation by adsorption on magnetic materials was performed, using pseudo-first-order, pseudo-second-order kinetic models, and intraparticle diffusion.

The pseudo-first-order kinetic model is mathematically expressed by the Equation (6):

$$Q_t = Q_e(1 - e^{-k_1 t}) \qquad (6)$$

where $k_1$ is pseudo-first-order rate adsorption constant (min$^{-1}$), and $Q_e$, $Q_t$ are the adsorption capacity at equilibrium and, respectively, the amount of CR/MO retained on the adsorbent at time $t$ (mg/g).

For the expression of the pseudo-second-order kinetic model, Equation (7) is used [32]:

$$Q_t = \frac{Q_e^2 k_2 t}{1 + Q_e k_2 t} \qquad (7)$$

where $k_2$ represents the rate constant of the pseudo-second-order adsorption process (g/mg·min);

$Q_e$, $Q_t$ are the adsorption capacity at equilibrium and, respectively, the amount of CR/MO retained on the adsorbent at time $t$ (mg/g).

Equation (8), presented in 1962 by Weber and Morris [33], is used to express the kinetic model of intraparticle diffusion:

$$Q_t = k_{id} t^{0.5} + C \qquad (8)$$

where $k_i$ is intraparticle diffusion rate constant (mg/g·min$^{0.5}$) and C (mg/g) defines intersection that provides indications regarding the thickness of the diffusion layer [33].

## 3. Results and Discussion

### 3.1. Materials Characterization

After synthesis, the prepared magnetic materials were characterized in terms of structure, texture, morphology, and magnetic properties. FTIR spectra of $CoFe_2O_4$ and $CoFe_2O_4$–Chit were recorded and discussed comparatively with the chitosan spectrum (Figure 2).

The FTIR spectrum of $CoFe_2O_4$ reveals the presence of two absorption bands (at 600 and 420 cm$^{-1}$) assigned to stretching and bending vibrations of the M–O bonds in tetrahedral and octahedral sites of spinel ferrites, respectively [34]. The presence of adsorbed water molecules is revealed by a very broad absorption band at 3398 cm$^{-1}$

(O–H stretching vibration mode) and by the band at 1629 cm$^{-1}$ corresponding to bending vibration of water molecules.
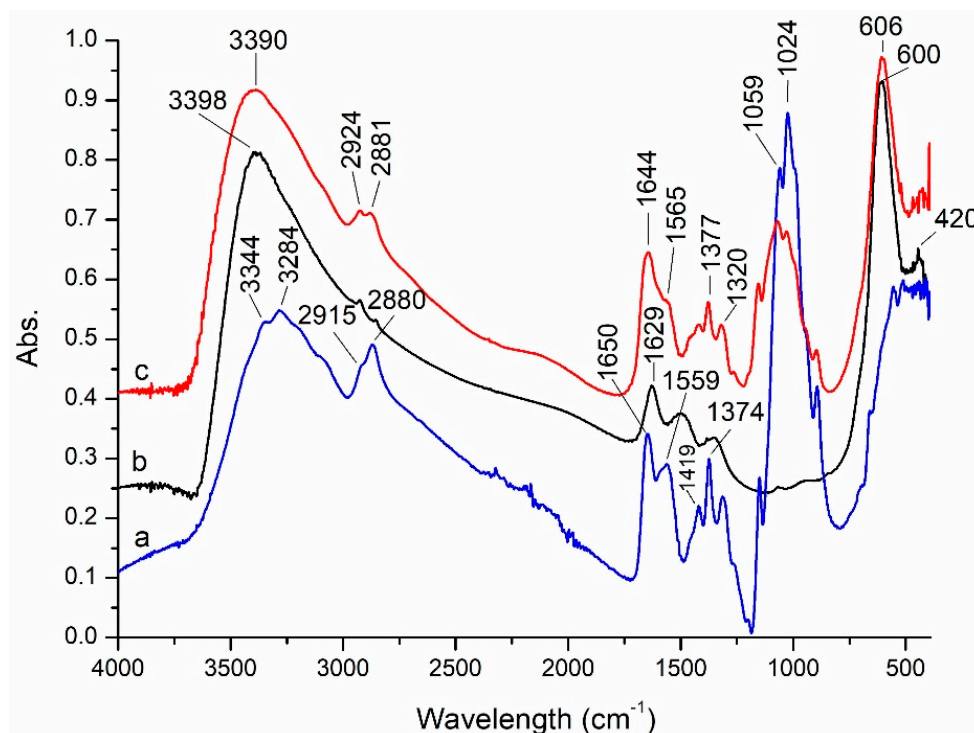


**Figure 2.** FTIR spectra of: (a) chitosan; (b) $CoFe_2O_4$; (c) $CoFe_2O_4$−Chit.

The FTIR spectrum of chitosan displays two absorption bands at 3344 and 3284 cm$^{-1}$ assigned to -OH and -NH$_2$ stretching vibrations, and two bands at 2915 cm$^{-1}$ due to the asymmetric C-H stretching vibrations and 2880 cm$^{-1}$ corresponding to symmetric C-H stretching vibrations. The peaks at 1650 and 1559 cm$^{-1}$ are related to the C=O stretching vibration of amide and the bending vibration of NH$_2$ groups, respectively [35]. The bands located at 1374 and 1024 cm$^{-1}$ are characteristic for C-O stretching vibration of C-OH [36] while that at 1419 cm$^{-1}$ is characteristic for –OH primary alcohol groups [37].

The absorption bands of chitosan are identified in the spectrum of $CoFe_2O_4$–Chit, but they are slightly shifted to lower or higher wavenumbers. These displacements indicate the involvement of the functional groups (-OH and -NH$_2$) of chitosan in coordination with the metallic ions of cobalt ferrite. The strong absorption peak at 606 cm$^{-1}$ related to the M-O vibrations of cobalt ferrite confirms the successful embedding of $CoFe_2O_4$ in the chitosan matrix.

The specific surface area ($S_{BET}$) of $CoFe_2O_4$ and $CoFe_2O_4$–Chit particles was determined by N$_2$ physisorption at −196 °C using the Brunauer–Emmett–Teller method. The $S_{BET}$ values were 199 m$^2$/g for cobalt ferrite and 2 m$^2$/g for cobalt ferrite–chitosan composite, respectively. There was a significant decrease in the specific surface area by preparing cobalt ferrite–chitosan composite as expected, taking into account that $CoFe_2O_4$–Chit was obtained as microspheres having a compact surface without porosity, as compared to $CoFe_2O_4$ which was obtained as a nanopowder. Figure 3 shows the nitrogen adsorption/desorption isotherm for $CoFe_2O_4$ that is of type IV according to the IUPAC classification, accompanied by a H2-type hysteresis loop. This type of isotherm and hysteresis is specific for mesoporous materials with a uniform porosity. The pore size distribution (inset of Figure 3) is monomodal and ranges between 2.5 and 6 nm with a peak maximum at ~3.5 nm.
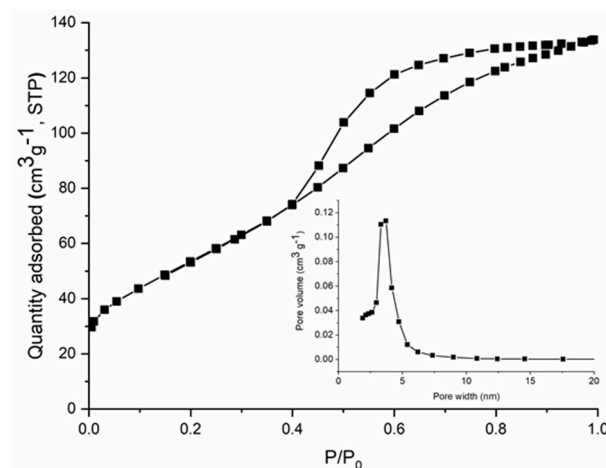
**Figure 3.** N$_2$ adsorption−desorption isotherms and pore size distribution (inset) of CoFe$_2$O$_4$.

The X-ray diffractograms of the prepared magnetic materials and free chitosan are presented in Figure 4.
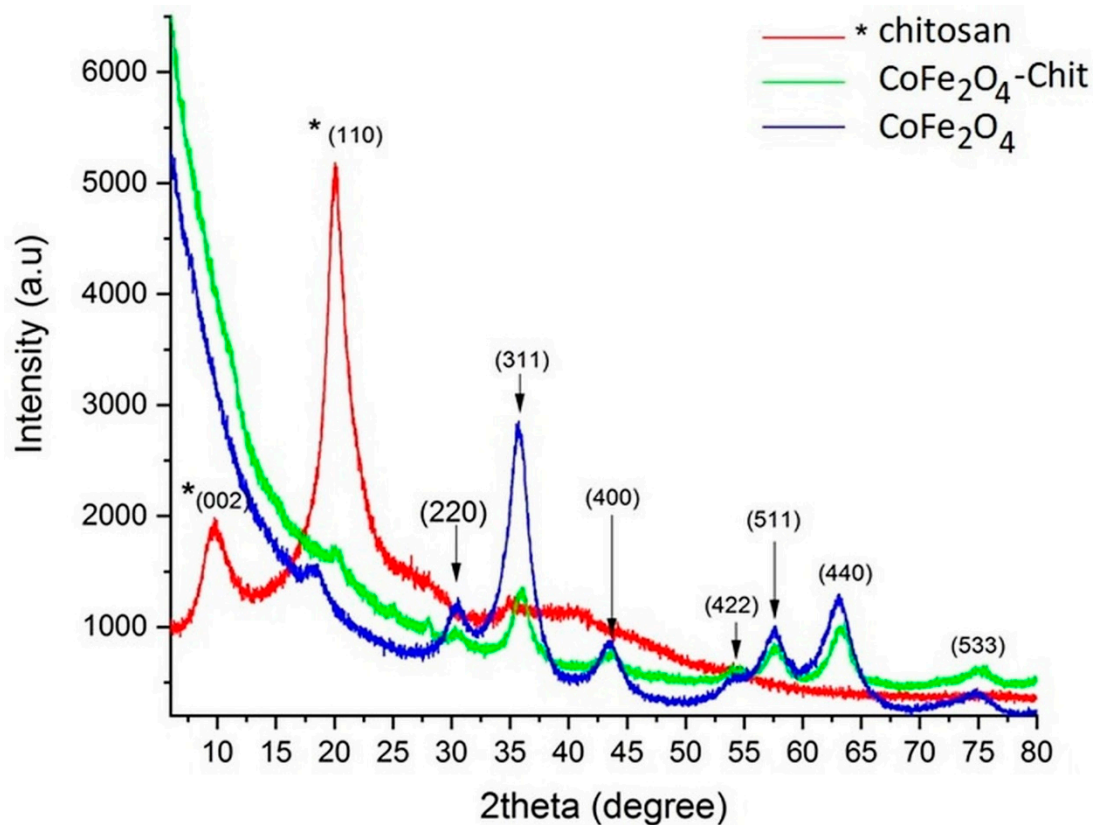


**Figure 4.** X-ray diffractograms of CoFe$_2$O$_4$, CoFe$_2$O$_4$–Chit, and Chitosan.

In the above diffractograms the families of crystalline planes (220), (311), (400), (511), (440) were identified corresponding to the cobalt ferrite CoFe$_2$O$_4$, (JCPDS no. 01-080-6487) metal oxide with a spinel-type structure that crystallizes in the cubic system, having the network constants a = b = c = 8.381 [Å] and cell Vol = 588.69 [Å$^3$]. In the case of our CoFe$_2$O$_4$ sample, the network constants a = b = c = 8.344 (6) and Vol = 580.84 and an average crystallite size were calculated with the Debye–Scherrer formula of approximately 4 nm (the average crystallite size was calculated using the Full with at Half Maximum

(FWHM) value corresponding to three diffraction maxima, after drawing a baseline and approximating the graph with the pseudo-Voigt function).

In the case of the X-ray diffractogram of chitosan, the crystalline planes (002) and (110) were identified at an angle of 2θ corresponding to the values of 9.68° and 20.05°; the average crystallite size is ≈3nm. These observations are in line with the literature data [38].

In the case of cobalt ferrite–chitosan composite, a significant decrease in the maximum intensity and an increase in the maximum diffraction width can be observed due to the phenomena induced by the very small particle size (a few nanometers) and the stress in the crystal lattice. In the case of $CoFe_2O_4$, a decrease in the network constant "a" and the volume of the elementary cell was observed. However, both crystallographic phases ($CoFe_2O_4$ and chitosan) are present and clearly distinguished.

TEM imaging of $CoFe_2O_4$ (Figure 5) revealed agglomerated nanoparticles (NPs) of ~3 nm in size, almost regular and spherical in shape. TEM observations also confirmed the porous structure of $CoFe_2O_4$. The Selected Area Electron Diffraction (SAED) correlated with the EDS results (Fe:Co ratio of 2:1) proved the $CoFe_2O_4$ phase of the NPs.
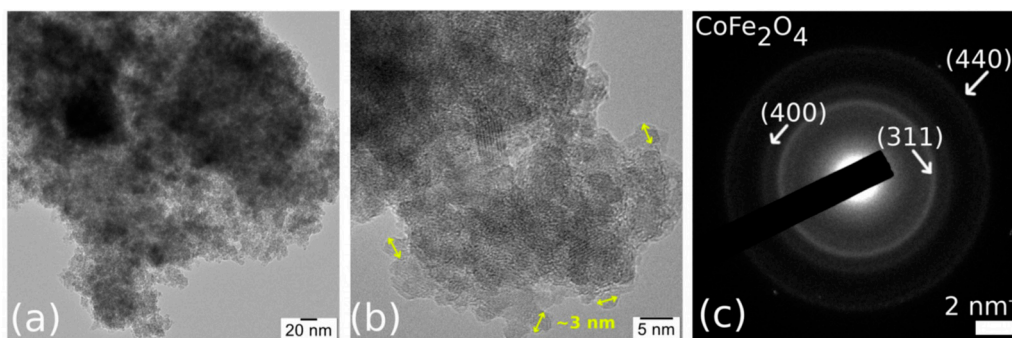


**Figure 5.** TEM image (**a**), High-Resolution Transmission Electron Microscopy (HRTEM) image (**b**), and Selected Area Electron Diffraction (SAED) (**c**) of the $CoFe_2O_4$ sample.

SEM images of $CoFe_2O_4$ (Figure 6) showed aggregates of nanoparticles with dimensions between 141 and 432 nm, but also larger aggregates (1.853 μm/2.428 μm/292.8 nm). The tendency of agglomeration of $CoFe_2O_4$ nanoparticles, attributed mainly to the higher interactions between nanoparticles, determined the formation of highly porous aggregates with higher adsorption capacity.
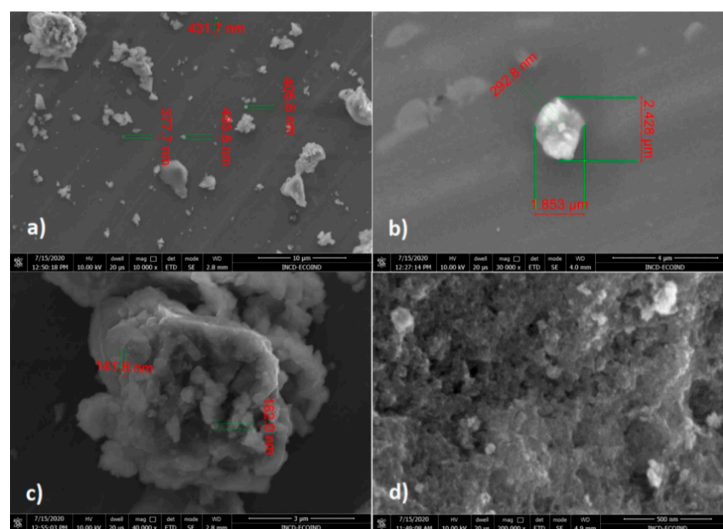


**Figure 6.** SEM images of $CoFe_2O_4$ at different magnifications: (**a**) 10.000×, (**b**) 30.000×, (**c**) 40.000×, (**d**) 200.000×.

Higher hemispherical particles with diameters between 804 μm and 1.41 mm have been observed for CoFe$_2$O$_4$–Chit (Figure 7). The shape and surface morphology of CoFe$_2$O$_4$–Chit particles is different compared to CoFe$_2$O$_4$. Thus, CoFe$_2$O$_4$–Chit is characterized by well-defined and smoother particles. Based on these observations it can be remarked that chitosan determined the decrease in the agglomeration tendency characteristic for CoFe$_2$O$_4$ nanoparticles.
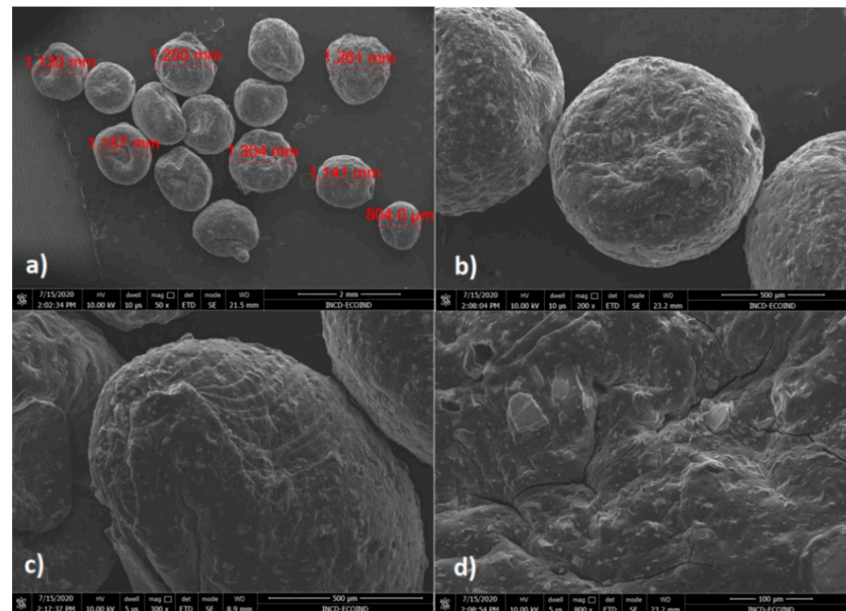


**Figure 7.** SEM images of CoFe$_2$O$_4$–Chit at different magnifications: (**a**) 50×, (**b**) 200×, (**c**) 300×, (**d**) 800×.

The magnetic properties of CoFe$_2$O$_4$ and CoFe$_2$O$_4$–Chit were measured on a VSM at room temperature by recording the magnetization versus applied field curves (Figure 8). Data presented in Figure 8a,b show no room temperature remanence or coercivity, thus revealing a superparamagnetic behavior of both samples. The experimental data were analyzed by fitting to the Langevin function. The saturation magnetization (Ms) values are 33.6 emu/g for CoFe$_2$O$_4$ and 8.4 emu/g for CoFe$_2$O$_4$–Chit. The decrease in Ms value of CoFe$_2$O$_4$–Chit compared to CoFe$_2$O$_4$ is due to the presence of the diamagnetic chitosan molecules.
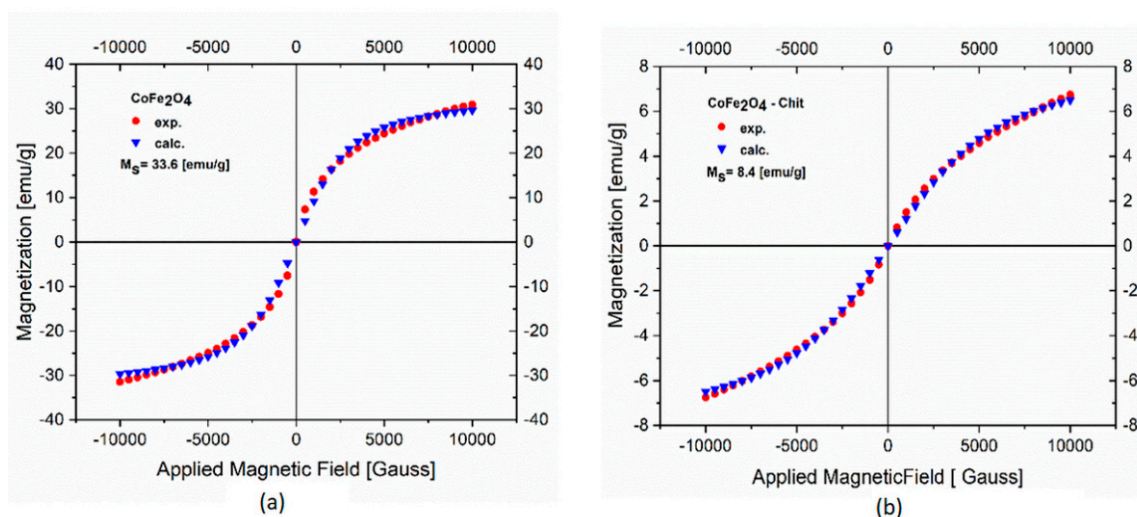


**Figure 8.** Magnetic hysteresis curves of CoFe$_2$O$_4$ (**a**) and CoFe$_2$O$_4$−Chit (**b**) at room temperature.

### 3.2. Adsorption Studies

The process of removing CR/MO by adsorption on $CoFe_2O_4$ and $CoFe_2O_4$–Chit was studied in batch experiments. The effect of some significant parameters on the retention capacity of these materials was considered. Among the parameters investigated, the following can be mentioned: pH, contact time, and concentration of CR/MO in the initial solution.

### 3.2.1. The pH Effect on Adsorption Capacity

pH is one of the great significant factors that influence the adsorption process of pollutants from aqueous effluents and wastewater. The pH influences the dyes' solubility in water, the activity of the functional sites on the surface of the adsorbents, and competition of ions for the adsorption centers.

To study the variation of $CoFe_2O_4$ and $CoFe_2O_4$–Chit adsorption capacity versus pH values, batch experiments were performed in the pH range of 2.22–10.8 using HCl and $NH_4OH$ solutions of various concentrations. A CR single solution of 102.81 mg/L (experimentally determined) and an MO single solution of 100 mg/L were used in the tests. The binary solutions CR/MO (100 mg/L CR + 100 mg/L MO) with a volume of 25 mL and 0.01 g of adsorbents were used to establish the pH effect on the adsorption capacity. The room temperature experiments were performed for 6 h to reach equilibrium. The experiments were carried out using single and binary dyes solutions at the same pH range. The experimental results regarding the effect of pH on CR/MO adsorption from single solutions are presented in Figure 9.
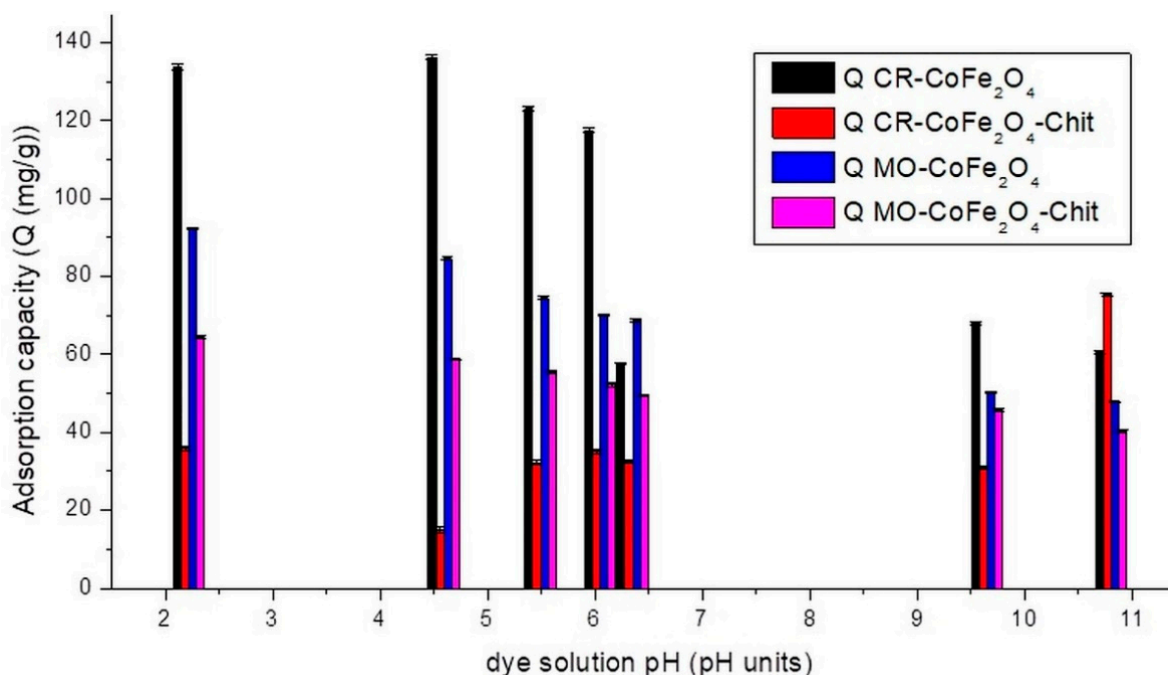


**Figure 9.** The variation of adsorption capacity versus the CR/MO solution's pH (single system).

Figure 9 reveals that in the case of CR adsorption, the studied magnetic materials are characterized by different behaviors. The adsorption capacity of $CoFe_2O_4$ decreases with the increase in dye solution pH from 2 to 11. This can be attributed to the fact that at low pH values, the positively charged $CoFe_2O_4$ surface interacts strongly with the negative sulfonate groups of the dyes. As the pH increases, the adsorption capacity starts to decrease because the surface of the adsorbent becomes less positive, while the molecules of adsorbate pass in the anionic form. The electrostatic repulsion forces become stronger in basic medium, thereby lowering the adsorption. The highest adsorption capacity of

$CoFe_2O_4$ was noticed at pH around 4.5. The adsorption behavior of $CoFe_2O_4$–Chit is slightly different. In an acidic pH range, the high concentration of protons determines the protonation of amine (-$NH_2$) and hydroxyl groups (-OH) of chitosan. These protonated functional groups will be electrostatically attracted by the negatively charged sulfonate groups of CR. Repulsive forces with protonated functional groups of Congo Red can also occur at low pH values (Figure 10).
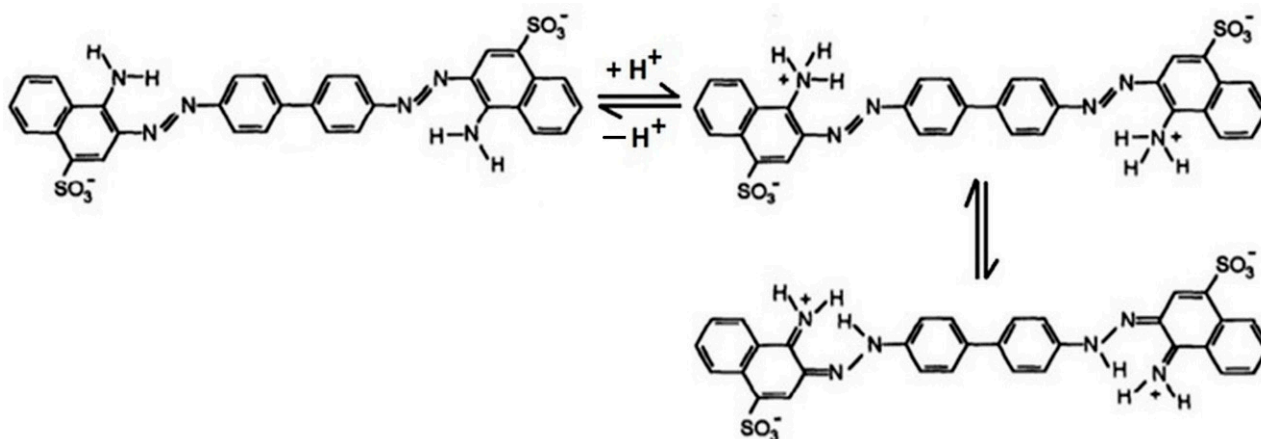


**Figure 10.** The Congo Red structures in acidic solution [39].

At higher pH values ranging from slightly acidic to neutral, where the chitosan surface is neutral the adsorption of the dye could also occur only by physical forces (hydrogen bonding and van der Waals forces) that will affect the adsorption capacity [39]. The highest value of adsorption capacity has been recorded at pH equal to 10.8. The literature data present similar behaviors related to the sorption properties of chitosan coated magnetic iron oxides [40]. Figure 9 shows that $CoFe_2O_4$ has a higher CR adsorption capacity than $CoFe_2O_4$–Chit. This is related mainly to the higher specific surface area of $CoFe_2O_4$ compared to $CoFe_2O_4$–Chit. On the other hand, the limited adsorption capacity of $CoFe_2O_4$–Chit could be attributed to the fact that during the synthesis of the composite, some functional groups of chitosan react with those of the $CoFe_2O_4$, the number of active sites available to interact with the dye molecules being reduced [41].

Taking into account these results, the further tests regarding adsorption capacity versus time for CR adsorption process were carried out at two pH values (4.5 and 10.8).

By analyzing Figure 9, it can be observed that the maximum adsorption capacity for MO of both adsorbents is at pH = 2.22 in single solutions. With the increase in pH values to 10.8, the adsorption capacity of $CoFe_2O_4$ and $CoFe_2O_4$-Chit decreases sharply. These results indicate that optimum pH value for the adsorption of MO onto $CoFe_2O_4$ and $CoFe_2O_4$–Chit in single solutions is 2.22. This can be attributed to strong electrostatic forces between anionic MO (pKa of MO 4.4–5.5) [42] and the positively charged $CoFe_2O_4$ surface under acidic conditions. The higher value of $CoFe_2O_4$–Chit under acidic conditions is based by the interactions between protonated amino groups of chitosan and sulfonate groups of MO [43]. At higher pH values, the high concentration of negative charges on the surface of both adsorbents inhibits the adsorption of the anionic MO.

Furthermore, it was also observed that both magnetic materials have lower adsorption capacity for MO compared to CR in single solutions, suggesting a higher selectivity of $CoFe_2O_4$ and $CoFe_2O_4$–Chit for CR in these conditions.

The effect of pH on MO/CR adsorption process in binary solution is presented in Figure 11.
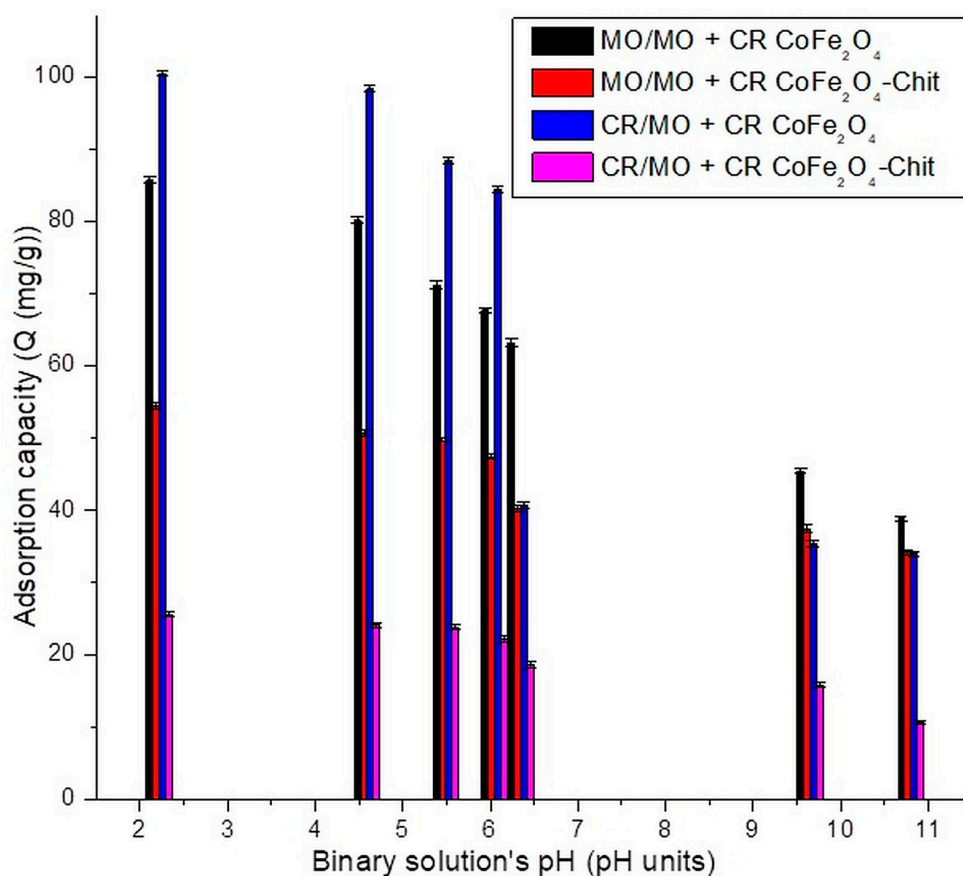
**Figure 11.** The variation of adsorption capacity versus CR/MO solution pH (binary system).

A similar behavior has been observed for the pH effect on adsorption capacity of dyes from binary solutions. For both magnetic materials, a decrease in the dyes' adsorption capacity was observed with the increase in pH value. A decrease in adsorption capacity was recorded in the experiments performed with binary dyes solutions. In case of CR, the maximum experimental adsorption capacity decreases with 35.63 mg/g for adsorption onto $CoFe_2O_4$ and with 49.75 mg/g for adsorption onto $CoFe_2O_4$–Chit from single to binary solutions. A lower decrease in the maximum experimental adsorption capacity was determined for MO (6.5 mg/g for adsorption onto $CoFe_2O_4$ and 39 mg/g for adsorption onto $CoFe_2O_4$–Chit from single to binary solutions). Therefore, at the same concentration, in binary solutions, MO has a more inhibitory effect on CR adsorption onto magnetic materials than CR on MO adsorption.

### 3.2.2. The Contact Time Effect on Adsorption Capacity

Contact time is a crucial operational parameter in the process of removing pollutants from wastewater and synthetic aqueous solutions. Batch experiments at room temperature and 150 rpm and different time periods (between 5 and 360 min) with volumes of 25 mL of 102.81 mg CR/L and 0.01 g $CoFe_2O_4$/$CoFe_2O_4$–Chit were performed to establish the equilibrium time.

The same experimental conditions were applied in tests for establishing the effect of contact time onto $CoFe_2O_4$/$CoFe_2O_4$–Chit adsorption capacity of MO and CR/MO from binary solutions.

The variation of the amount of dye retained per gram of $CoFe_2O_4$/$CoFe_2O_4$–Chit versus contact time is illustrated in Figures 12–14.
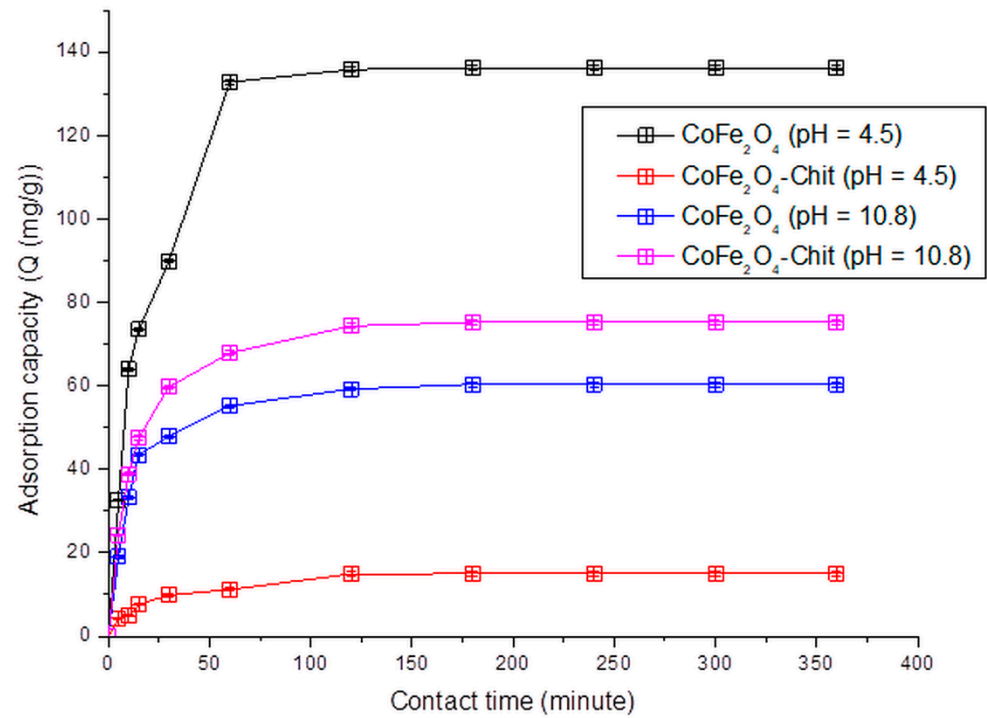
**Figure 12.** The variation of $CoFe_2O_4/CoFe_2O_4$–Chit adsorption capacity versus contact time at pH = 4.5 and pH = 10.8 for the CR adsorption process.
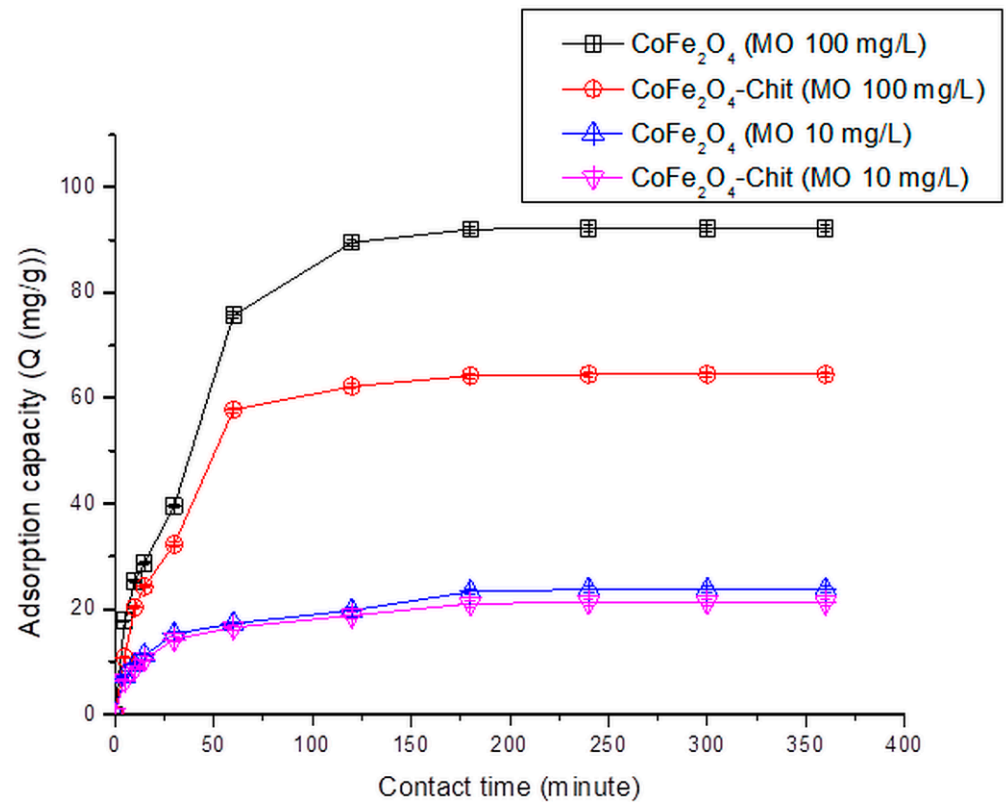


**Figure 13.** The variation of $CoFe_2O_4/CoFe_2O_4$–Chit adsorption capacity versus contact time at pH = 2.22 for the MO adsorption process (pH = 2.22).
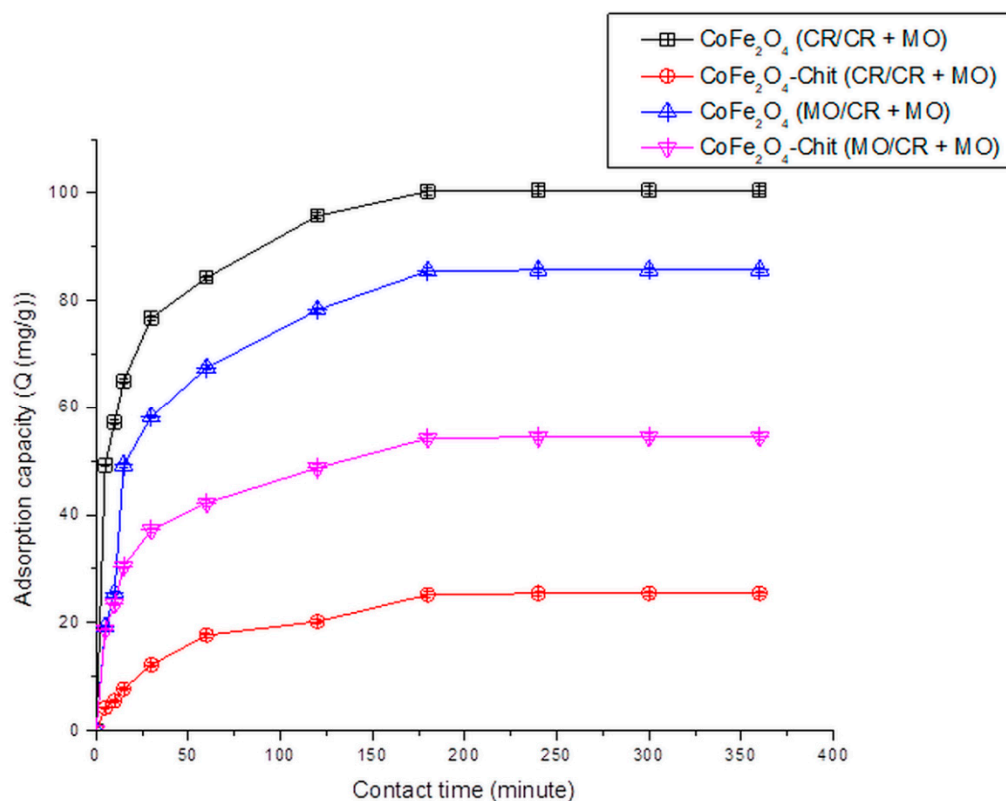
**Figure 14.** The variation of $CoFe_2O_4$/$CoFe_2O_4$–Chit adsorption capacity versus contact time for the CR and MO adsorption from binary solution (100mg/L CR + 100 mg/L MO) (pH = 2.22).

It can be stated that the process of CR and MO retaining onto $CoFe_2O_4$/$CoFe_2O_4$–Chit takes place in two stages. In the first phase occurring in the first 30 min, the amount of retained CR/MO rapidly increases due to the fact that during this period the surface of the adsorbents has a large number of active centers available for retaining CR/MO (pollutant). The same finding is valid for the adsorption process of CR and MO from binary solutions.

As the contact time increases, the number of free active centers decreases, and consequently the speed of the retention process decreases. In our case, the equilibrium time is approximately 180 min for CR adsorption and 240 min for MO adsorption from single and binary solutions.

It can also be seen from the Figure 12 that the value of the maximum CR adsorption capacity experimentally determined is 136.13 mg/g for $CoFe_2O_4$ and 75.25 mg/g for $CoFe_2O_4$–Chit. Figure 13 reveals that the value of the maximum MO adsorption capacity experimentally determined is 92.2 mg/g for $CoFe_2O_4$ and 64.5 mg/g for $CoFe_2O_4$–Chit. These values are lower for binary solutions (Figure 14). Thus, the maximum CR adsorption capacity experimentally determined decreases to 100.5 mg/g for $CoFe_2O_4$ and 25.5 mg/g for $CoFe_2O_4$-Chit, while the maximum MO adsorption capacity experimentally determined decreases to 85.7 mg/g for $CoFe_2O_4$ and 54.5 mg/g for $CoFe_2O_4$–Chit, respectively.

These values are consistent with the size of the adsorbent particles and the specific surface areas. Cobalt ferrite was obtained as a nanopowder with specific surface area of about 199 $m^2$/g, while $CoFe_2O_4$–Chit ferrite was obtained as microparticles with a specific surface area of about 2 $m^2$/g.

### 3.2.3. The Isothermal Study
Single Component Adsorption Isotherm Study

The experimental results of the dyes' adsorption process on $CoFe_2O_4$/$CoFe_2O_4$–Chit from single-component solutions were fitted with Langmuir and Freundlich isotherm models (Figures 15 and 16).

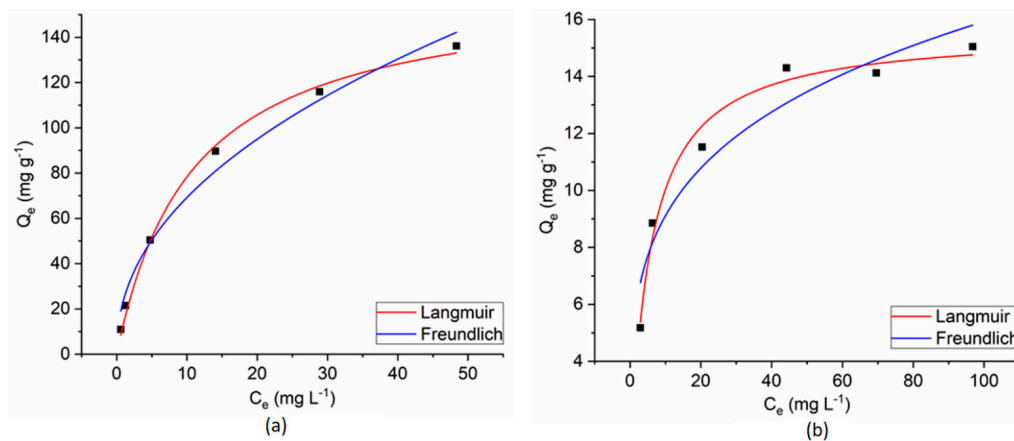**Figure 15.** Langmuir and Freundlich fitting curves for CR adsorption onto $CoFe_2O_4$ (**a**) and $CoFe_2O_4-Chit$ (**b**) from a single component solution.
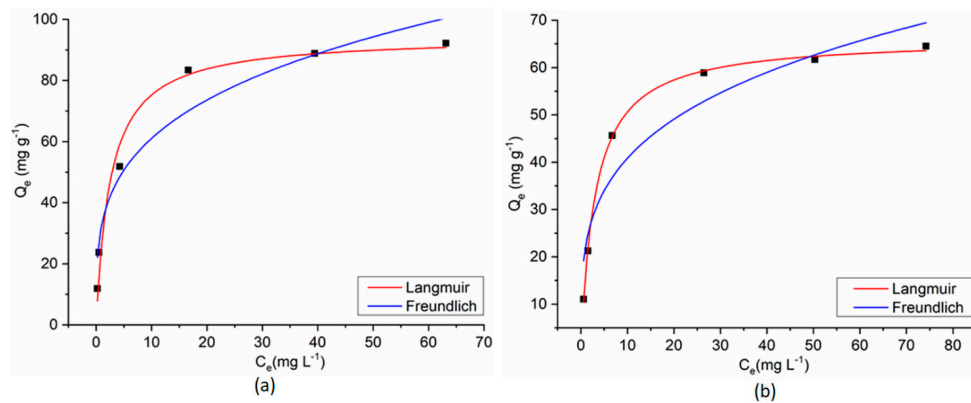


**Figure 16.** Langmuir and Freundlich fitting curves for MO adsorption onto $CoFe_2O_4$ (**a**) and $CoFe_2O_4-Chit$ (**b**) from single component solution.

The Langmuir isotherm model assumes a monolayer adsorption on a homogeneous surface. Consequently, all the adsorption centers are identical [32].

The Freundlich isotherm describes a multilayer adsorption on a heterogeneous and non-uniform surface [32].

The equilibrium isotherm parameters and the correlation coefficients ($R^2$) for the studied adsorption processes are presented in Table 1.

**Table 1.** Langmuir and Freundlich parameters for the dyes' adsorption onto $CoFe_2O_4$ and $CoFe_2O_4$–Chit from single-component solutions.

| Dye | CR | | MO | |
|---|---|---|---|---|
| **Sample** | **$CoFe_2O_4$** | **$CoFe_2O_4$-Chit** | **$CoFe_2O_4$** | **$CoFe_2O_4$–Chit** |
| Langmuir Parameters | | | | |
| $Q_{max}$ (mg/g) | $162.676 \pm 6.0642$ | $15.6042 \pm 0.4257$ | $94.4626 \pm 4.6652$ | $66.1876 \pm 0.5552$ |
| $K_L$ (L/mg) | $0.0928 \pm 0.0104$ | $0.1800 \pm 0.0233$ | $0.3921 \pm 0.1071$ | $0.3251 \pm 0.0138$ |
| $R^2$ | 0.9964 | 0.9834 | 0.9711 | 0.9988 |
| AIC | 30.37 | 8.51 | 36.93 | 12.23 |
| $R_L$ | 0.100 | 0.050 | 0.025 | 0.030 |
| Freundlich Parameters | | | | |
| $K_F$ (mg/g) | $24.1787 \pm 3.6051$ | $5.2154 \pm 0.8263$ | $32.8071 \pm 5.5190$ | $22.2068 \pm 4.3014$ |
| 1/n | $0.4568 \pm 0.0437$ | $0.2424 \pm 0.0410$ | $0.2698 \pm 0.0480$ | $0.2647 \pm 0.0530$ |
| $R^2$ | 0.9830 | 0.9226 | 0.9236 | 0.8939 |
| AIC | 39.68 | 17.75 | 42.77 | 39.52 |

For the Langmuir isotherm, a dimensionless separation factor ($R_L$) can be estimated with Equation (9):

$$R_L = \frac{1}{(1 + K_L \times C_0)} \tag{9}$$

where $C_0$ is the highest initial concentration of dye (mg/L);

$K_L$ is adsorption constant for Langmuir model (L/mg).

The $R_L$ value can be used to determine whether the Langmuir model favorably describes the adsorption process. A value of $R_L > 1$ indicates that the adsorption is not favorable; if $R_L = 1$, the adsorption is linear; for $0 < R_L < 1$, the adsorption is favorable, and if $R_L = 0$, it means that adsorption is irreversible [33].

The goodness of fit of the experimental data has been verified by the calculation of the correlation coefficient ($R^2$) and the Akaike's Information Criterion (AIC). Lower AIC values (on a scale from $-\infty$ to $+\infty$) demonstrate that the respective model is more likely to characterize the sorption process than the alternative model [44].

As can be seen in Table 1, the correlation coefficients ($R^2$) and AIC values reveal that all the adsorption data fit better with the Langmuir isotherm model. These results suggest that adsorption of both dyes on the studied magnetic materials from single-component solutions takes place as a monolayer adsorption process on a homogeneous surface. The $R_L$ values, between 0 and 1, support the favorability of the adsorption reaction and confirm that electrostatic interactions between magnetic adsorbents and dye molecules.

Competitive Adsorption of CR and MO in Binary Solutions

For a binary mixture containing CR and MO, the adsorption capacity of CR can be determined using the modified Langmuir isotherm model, mathematically expressed by the Equation (10) [45]:

$$Q_{e,CR} = \frac{Q_{max,CR} K_{L,CR} C_{e,CR}}{1 + K_{L,CR} C_{e,CR} + K_{L,MO} C_{e,MO}} \tag{10}$$

The linearization form of this model is given by Equation (11):

$$\frac{1}{Q_{e,CR}} = \frac{1}{Q_{max,CR}} + \frac{1}{Q_{max,CR} K_{L,CR}} \left[ \frac{1}{C_{e,CR}} + \frac{K_{L,MO} C_{e,MO}}{C_{e,CR}} \right] \tag{11}$$

To estimate MO adsorption capacity in the binary mixture, Equation (9) was rewritten as shown in Equation (12).

$$\frac{1}{Q_{e,MO}} = \frac{1}{Q_{max,MO}} + \frac{1}{Q_{max,MO} K_{L,MO}} \left[ \frac{1}{C_{e,MO}} + \frac{K_{L,CR} C_{e,CR}}{C_{e,MO}} \right] \tag{12}$$

where $C_{e,CR}$, $C_{e,MO}$, $Q_{e,CR}$, and $Q_{e,MO}$ are equilibrium concentration and equilibrium adsorption capacity of *CR* and *MO* in the binary solution, $K_{L,CR}$ and $K_{L,MO}$ are Langmuir constants obtained in singe dye systems, $Q_{max,CR}$ and $Q_{max,MO}$ are maximum adsorption capacity of CR and MO in the binary solution.

Substituting the values of $C_{e,CR}$, $C_{e,MO}$, $Q_{e,CR}$, $K_{L,CR}$, and $K_{L,MO}$ in Equation (11) and making a linear plot of $\frac{1}{Q_{e,CR}}$ versus $\left[ \frac{1}{C_{e,CR}} + \frac{K_{L,MO} C_{e,MO}}{C_{e,CR}} \right]$ (Figure S5), one can obtain $Q_{max,CR}$ in the binary solution. $Q_{max,MO}$ can be calculated by the same procedure using the Equation (12).

According to Mahamadi et al. [46], the ratio between $Q_{max,binary}$ and $Q_{max,single}$ gives information regarding the adsorption dynamics in binary solutions. When this ratio is >1, the two adsorbates have a synergistic behavior, the effect of the mixture being greater than the effect of the individual adsorbates in the mixture. When the ratio is <1, the two adsorbates have an antagonistic behavior, the effect of the mixture being less than that of each of the individual adsorbates in the mixture. When the ratio = 1, the mixture has no effect on the adsorption of each of the adsorbates in the mixture. The $Q_{max,binary}/Q_{max,single}$

ratios for the adsorption of CR and MO onto $CoFe_2O_4$ and $CoFe_2O_4$–Chit are presented in Table 2.

**Table 2.** Maximum adsorption capacity calculated using Langmuir and modified Langmuir isotherm models for single-component and binary solutions.

| Adsorbent | Dye | Parameters | Single Component Solution (mg/g) | Binary Solution (mg/g) | $Q_{max,binary}/Q_{max,single}$ |
|---|---|---|---|---|---|
| $CoFe_2O_4$ | CR | $Q_{max,CR}$ | 162.67 | 79.87 | 0.49 |
| | MO | $Q_{max,MO}$ | 94.46 | 117.50 | 1.24 |
| $CoFe_2O_4$-Chit | CR | $Q_{max,CR}$ | 15.60 | 25.32 | 1.62 |
| | MO | $Q_{max,MO}$ | 66.18 | 81.30 | 1.22 |

The $Q_{max,binary}/Q_{max,single}$ ratio is <1 only in the case of CR adsorption onto $CoFe_2O_4$, suggesting that the adsorption of this dye onto $CoFe_2O_4$ is hindered by the presence of MO. The effect of the mixture seems to be synergistic in the case of adsorption of both dyes onto $CoFe_2O_4$–Chit and for MO onto $CoFe_2O_4$. This behavior can be attributed to the size of the dye molecules and the texture of the adsorbent. As the CR molecules are much larger than those of MO, it is expected that their adsorption on $CoFe_2O_4$ with a porous structure (pore diameters ranging from 2.5 to 6 nm) will be hindered by the presence of MO molecules in a binary solution. In the case of MO adsorption on $CoFe_2O_4$ from a binary solution, the CR molecules, being larger, cannot penetrate as easily into the porous network of the adsorbent; therefore, they do not depress the MO adsorption. On the contrary, they have a synergistic effect. In the case of $CoFe_2O_4$–Chit which is not porous, the adsorption of the dyes is not influenced by the mutual presence of both components in solution because the process occurs on the external surface of the adsorbent.

Comparing the maximum adsorption capacities of both magnetic adsorbents included in this study with those reported in the literature for other magnetic materials, one can notice that they present comparable or even higher values (Table 3).

**Table 3.** Adsorption capacities of different magnetic adsorbents from the literature for the removal of CR and MO.

| Dye | Adsorbent | Adsorption Capacity (mg/g) | Reference |
|---|---|---|---|
| CR | $Fe_3O_4$@$SiO_2$@ZnTDPAT | 17.73 | [47] |
| | m-Cell/$Fe_3O_4$/ACCS | 66.1 | [48] |
| | $MgFe_2O_4$-$NH_2$ NPs | 71.4 | [49] |
| | $Fe_3O_4$@$SiO_2$@MgAl-borate LDH | 158.98 | [50] |
| | $Fe_xCo_{3-x}O_4$ | 128.6 | [51] |
| | Chitosan/iron oxide nanocomposite films | 25.5 | [40] |
| | Chitosan/iron oxide nanocomposite films prepared by sonication | 700 | [40] |
| | $CoFe_2O_4$ | 162.68 | This study |
| | $CoFe_2O_4$–Chit | 15.60 | This study |
| | $CoFe_2O_4$ from binary solutions with MO | 79.87 | This study |
| | $CoFe_2O_4$-Chit from binary solutions with MO | 25.32 | This study |
| MO | Muscovite supported $Fe_3O_4$ nanoparticles | 149.25 | [52] |
| | Multi-walled carbon nanotubes (MWCNTs) coated with magnetic $ZnLa_{0.02}Fe_{1.98}O_4$ clusters | 81 | [53] |
| | Mesoporous $Fe_3O_4$–$SiO_2$–$TiO_2$ (MFST) | 2.5 | [54] |
| | Magnetic iron oxide/carbon nanocomposites | 72.68 | [55] |
| | Magnetic iron oxide/carbon nanocomposites from binary solutions with phenol | 71.02 | [56] |
| | Rectorite/iron oxide nanocomposites | 0.36 | [56] |
| | $\gamma$-$Fe_2O_3$/$SiO_2$/chitosan composite | 34.29 | [57] |
| | $CoFe_2O_4$ | 94.46 | This study |
| | $CoFe_2O_4$–Chit | 66.18 | This study |
| | $CoFe_2O_4$ from binary solutions with CR | 117.50 | This study |
| | $CoFe_2O_4$–Chit from binary solutions with CR | 81.30 | This study |

### 3.2.4. The Kinetic Study

Pseudo-first-order, pseudo-second-order, and the intraparticle diffusion kinetic models were applied to determine the controlling mechanism of dye adsorptions from aqueous solution. Graphical representations of these kinetic models are displayed in Figures S6–S14, and the calculated kinetic parameters and values of regression coefficients are presented in Table 4.

**Table 4.** The kinetic parameters for the dyes' adsorption onto $CoFe_2O_4$ and $CoFe_2O_4$–Chit obtained by nonlinear regression of the experimental data.

| Sample | CR-$CoFe_2O_4$ | CR-$CoFe_2O_4$-Chit | MO-$CoFe_2O_4$ | MO-$CoFe_2O_4$-Chit |
|---|---|---|---|---|
| Single solutions | | | | |
| $Q_e$ exp (mg/g) | 136.13 | 15.04 | 92.20 | 64.50 |
| Pseudo-first-order model | | | | |
| $k_1$ (min$^{-1}$) | $0.0497 \pm 0.0043$ | $0.0396 \pm 0.0049$ | $0.0247 \pm 0.0022$ | $0.0301 \pm 0.0024$ |
| $Q_e$ cal (mg/g) | $135.69 \pm 2.77$ | $14.75 \pm 0.44$ | $92.86 \pm 2.14$ | $64.59 \pm 1.27$ |
| $R^2$ | 0.9843 | 0.9693 | 0.9868 | 0.9892 |
| AIC | 48.38 | 7.184 | 39.82 | 29.48 |
| Pseudo-second-order model | | | | |
| $k_2$ ($10^{-3}$ g/mg·min) | $0.4731 \pm 0.1000$ | $3.2750 \pm 0.9000$ | $0.2775 \pm 0.1000$ | $0.5131 \pm 0.2000$ |
| $Q_e$ cal (mg/g) | $146.55 \pm 8.55$ | $16.18 \pm 0.94$ | $106.05 \pm 8.98$ | $72.47 \pm 5.34$ |
| $R^2$ | 0.9832 | 0.9862 | 0.9782 | 0.9806 |
| AIC | 49.12 | $-1.60$ | 45.34 | 35.93 |
| Intraparticle diffusion model | | | | |
| $k_i$ | 8.89 | 1.01 | - | - |
| $R^2$ | 0.8296 | 0.9278 | - | - |
| Binary solutions | | | | |
| $Q_e$ exp (mg/g) | 100.50 | 64.50 | 23.75 | 21.25 |
| Pseudo-first-order model | | | | |
| $k_1$ (min$^{-1}$) | $0.0899 \pm 0.0143$ | $0.0301 \pm 0.0024$ | $0.0439 \pm 0.0072$ | $0.0471 \pm 0.0062$ |
| $Q_e$ cal (mg/g) | $95.39 \pm 3.29$ | $64.59 \pm 1.27$ | $22.34 \pm 0.88$ | $20.27 \pm 0.63$ |
| $R^2$ | 0.8267 | 0.9843 | 0.8994 | 0.9325 |
| AIC | 51.18 | 29.18 | 23.10 | 16.78 |
| Pseudo-second-order model | | | | |
| $k_2$ ($10^{-3}$ g/mg·min) | $1.3470 \pm 0.3698$ | $0.5131 \pm 0.1754$ | $2.3590 \pm 1.0000$ | $2.8520 \pm 1.0000$ |
| $Q_e$ cal (mg/g) | $101.22 \pm 4.90$ | $72.47 \pm 5.75$ | $24.51 \pm 1.60$ | $22.11 \pm 0.92$ |
| $R^2$ | 0.9569 | 0.9682 | 0.9651 | 0.9847 |
| AIC | 37.28 | 35.05 | 11.35 | 0.73 |

Analyzing the results, it can be noticed that in the case of single-component solutions, the correlation coefficients $R^2$ for the pseudo-first-order and pseudo-second-order kinetic models have close values regardless of adsorbate and adsorbent. Therefore, using a nonlinear method, both pseudo-first-order and pseudo-second-order kinetics represent well the kinetics of the adsorption process. Taking into account the AIC parameter and the fact that calculated $Q_e$ values are much closer to those determined experimentally in the case of pseudo-first-order kinetic model, it can be said that this model describes somewhat better the adsorption process in single-component solutions.

In binary solutions it can be noticed that adsorption of CR/MO on $CoFe_2O_4$ follows better the pseudo-second-order kinetics model as the $R^2$ coefficients are higher and the AIC values are smaller than those calculated for pseudo-first-order model. The adsorption process of CR/MO on $CoFe_2O_4$–Chit seems to respect the kinetic behavior identified for single-component solutions.

Furthermore, it can be observed (from Figures S10 and S13) that for MO adsorption and CR/MO adsorption from binary solutions, the curve that describes the intraparticle diffusion kinetic model can be fragmented into three lines with individual slopes, but the lines do not pass through the origin. According to this model, if the plot is multilinear or

does not pass through the origin, the process of adsorption is controlled by two or more diffusion mechanisms with different rate constants [58]. The literature data indicate that the first section of the curve can be attributed to the bulk diffusion; the linear section is characteristic to the intraparticle diffusion and the plateau to the equilibrium [59]. This means that in our case the adsorption process occurs in phases, and pore diffusion may not be considered as the sole operating rate-controlling step.

### 3.2.5. Desorption Study

One of the most important properties of any adsorbent is related to its regeneration capacity and possibility to be used in multi-cycle systems. These properties influence the performance of the adsorbents and the total operational cost of the adsorption process. In our case, acetone and ethanol were designated as desorbing agents in order to test the reusability of $CoFe_2O_4$ and $CoFe_2O_4$–Chit in multiple dye adsorption–desorption cycles. The reason of their choice was their high dipole moments [60]. Five adsorption–desorption cycles in acetone and ethanol were applied to check the reusability of both adsorbents. The results of these experiments are presented in Figure 17a,b.
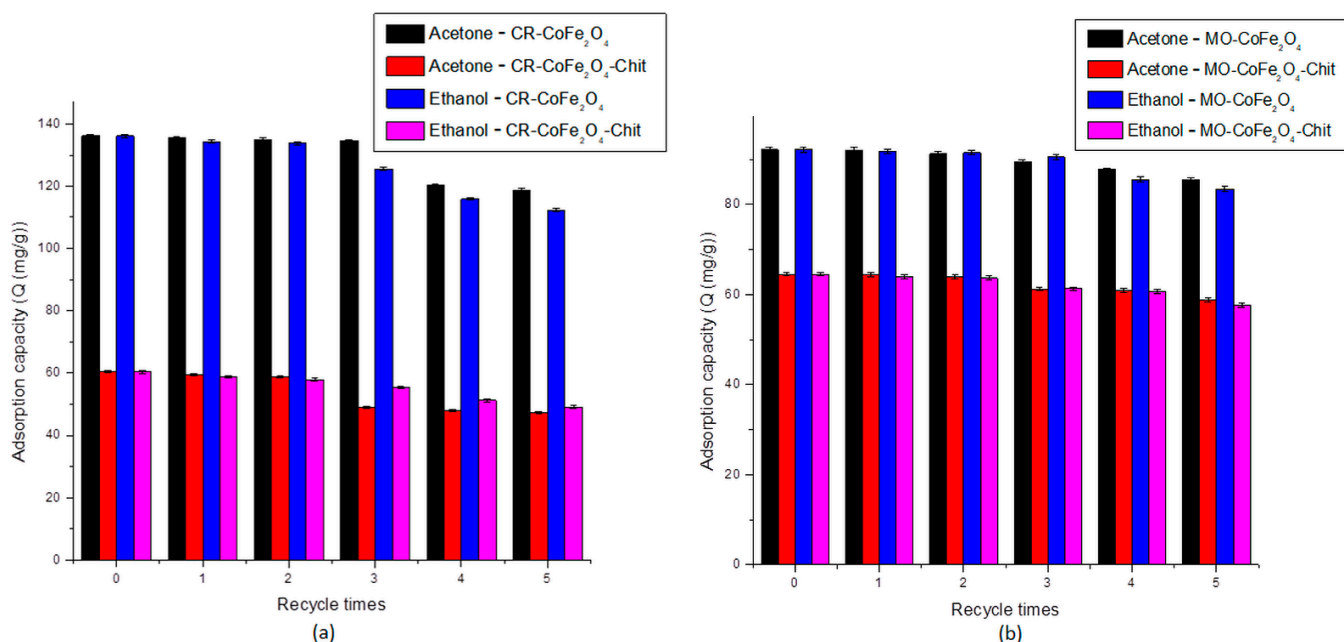


**Figure 17.** Reusability of $CoFe_2O_4$ and $CoFe_2O_4$−Chit for CR (**a**) and MO (**b**).

As shown in Figure 17a,b, the adsorption capacity was maintained at the same level after three cycles of adsorption–desorption for both desorbing agents tested. A slight decrease in the adsorption capacity was observed after five consecutive runs: the adsorption capacity of $CoFe_2O_4$ decreased by 12.75% for CR and 7.35% for MO by the use of acetone as a desorbing agent. A higher decrease has been recorded by using ethanol as a desorbing agent (17.47% for CR and 9.50% for MO). A similar conclusion can be drawn from the experiments performed for $CoFe_2O_4$–Chit. In the case of CR, we observed a decrease by 21.81% and 18.73% by the use of acetone and ethanol, respectively. A lower decrease in the adsorption capacity of $CoFe_2O_4$–Chit was noticed after five MO adsorption–desorption cycles: 8.88% by the use of acetone and 10.60% by the use of ethanol. These values revealed that after five adsorption–desorption cycles, the adsorption capacities are still at high level.

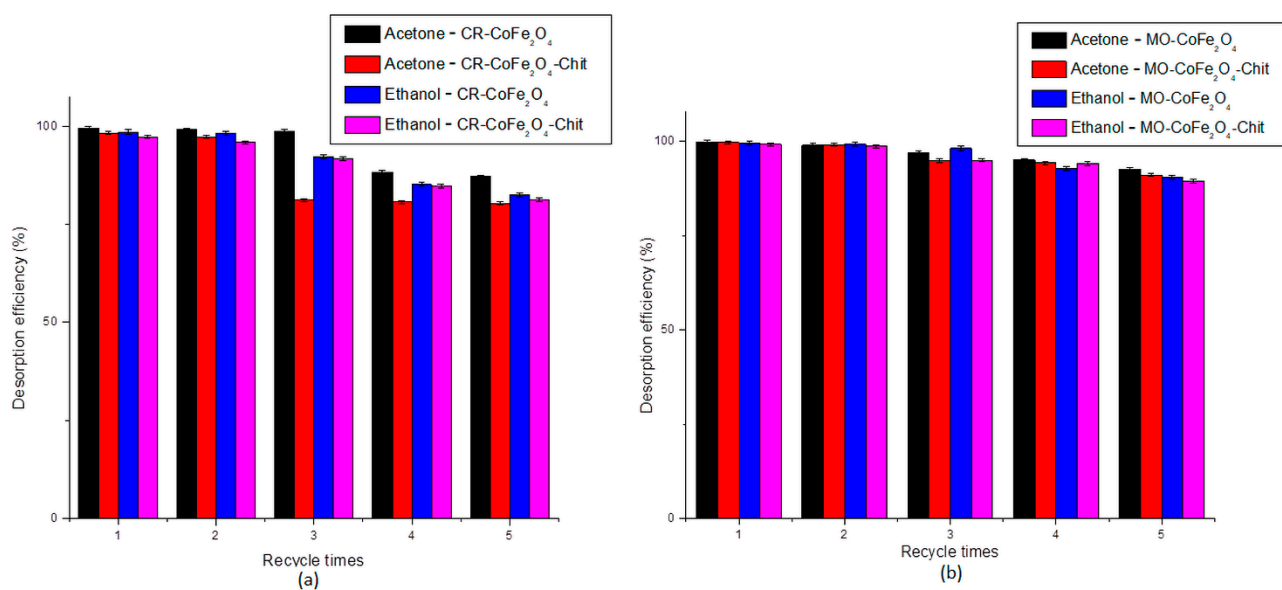Figure 18 shows the desorption efficiency behavior for all five cycles of adsorption-desorption.

**Figure 18.** Desorption efficiency of acetone and ethanol for CR (**a**) and MO (**b**).

The results showed that both desorbing agents have similar desorption efficiency. The desorption efficiency of acetone varied between 99.5 and 80.33%, while the desorption efficiency of ethanol varied between 99.44 and 81.27%. After five adsorption–desorption consecutive cycles, both adsorbents lost 18–19% of the desorption efficiency.

Thus, it can be said that both magnetic materials can be effective adsorbent materials for the remediation of dye-polluted waters.

## 4. Conclusions

Cobalt ferrite and cobalt ferrite–chitosan composite were synthesized by a simple coprecipitation method to be used as effective adsorbents for removal of Congo Red and Methyl Orange dyes from single and binary aqueous solutions. The as-obtained magnetic materials prepared were characterized by FTIR spectroscopy, specific surface area and porosity analysis, SEM and TEM analysis, X-Ray diffraction, and magnetic measurements. The results confirmed the successful synthesis of magnetic materials.

The optimal parameters of the CR/MO retention process on the prepared cobalt ferrite/cobalt ferrite–chitosan composite were determined from batch experiments at room temperature in single and binary dye solutions. It was found that the adsorption process depends on pH, time, initial concentration of CR/MO, and the presence of competing dye. The amount of CR/MO retained per gram of adsorbent material increases with increasing initial CR/MO concentration and contact time until equilibrium is reached. Experimental data were correlated with the most commonly used models of adsorption isotherms to describe the adsorption processes. The Langmuir isotherm best describes the adsorption on both adsorbents and indicates that CR/MO adsorption occurs on the homogeneous surface of cobalt ferrite and cobalt ferrite–chitosan composite as a monolayer. The values of adsorption capacity are higher for cobalt ferrite than cobalt ferrite–chitosan composite. These values are consistent with the size and specific surface areas of the adsorbent particles. Additionally, the values of maximum adsorption capacity for cobalt ferrite revealed that this adsorbent is selective for CR, while cobalt ferrite–chitosan composite is selective for MO.

Kinetic modeling, by the non-linear method, demonstrates that the kinetics of the adsorption process of CR/MO on cobalt ferrite/cobalt ferrite–chitosan composite are different in single-component and binary solutions. Pore diffusion might have significant influence on the kinetics of the process. Acetone and ethanol can be successfully used as desorbing agents, the adsorption capacities of the magnetic materials having a small decline after five adsorption–desorption cycles.

The results of the study indicate that cobalt ferrite and cobalt ferrite–chitosan composite are relevant as magnetic adsorbents to clean dye-containing wastewater.

**Supplementary Materials:** The following are available online at https://www.mdpi.com/2079-4991/11/3/711/s1, Figure S1: UV-Vis absorption spectra of CR obtained by HPLC-DAD; Figure S2: UV-Vis absorption spectra of Methyl Orange obtained by HPLC-DAD; Figure S3: HPLC-DAD calibration curve of Congo Red; Figure S4: HPLC-DAD calibration curve of Methyl Orange; Figure S5: The modified Langmuir isotherm model for (a) CR in binary solution (CR + MO) and (b) MO in binary solution (CR + MO); Figure S6: Graphical representation of the pseudo-first order kinetic model for removal of CR by adsorption on $CoFe_2O_4$ and $CoFe_2O_4$–Chit (nonlinear regression); Figure S7: Graphical representation of the pseudo-second order kinetic model for removal of CR by adsorption on $CoFe_2O_4$ and $CoFe_2O_4$–Chit (nonlinear regression); Figure S8: Graphical representation of the intraparticle diffusion model for the process of removal of CR by adsorption on $CoFe_2O_4$ and $CoFe_2O_4$–Chit; Figure S9: Graphical representation of the pseudo-first order kinetic model for removal of MO by adsorption on $CoFe_2O_4$ and $CoFe_2O_4$–Chit (nonlinear regression); Figure S10 Graphical representation of the pseudo-second order kinetic model for removal of MO by adsorption on $CoFe_2O_4$ and $CoFe_2O_4$–Chit (nonlinear regression); Figure S11: Graphical representation of the intraparticle diffusion model for the process of removal of MO by adsorption on $CoFe_2O_4$ and $CoFe_2O_4$–Chit; Figure S12: Graphical representation of the pseudo-first order kinetic model for removal of CR and MO by adsorption on $CoFe_2O_4$ and $CoFe_2O_4$–Chit from binary dye solutions (nonlinear regression); Figure S13: Graphical representation of the pseudo-second order kinetic model for removal of CR and MO by adsorption on $CoFe_2O_4$ and $CoFe_2O_4$–Chit from binary dye solutions (nonlinear regression); Figure S14: Graphical representation of the intraparticle diffusion kinetic model for removal of CR and MO by adsorption on $CoFe_2O_4$ and $CoFe_2O_4$–Chit from binary dye solutions.

## References

1. Nghiem, L.D.; Schäfer, A.I.; Elimelech, M. Pharmaceutical retention mechanisms by nanofiltration membranes. *Environ. Sci. Technol.* **2005**, *39*, 7698–7705. [CrossRef] [PubMed]
2. Zhou, Y.; Lu, J.; Zhou, Y.; Liu, Y. Recent advances for dyes removal using novel adsorbents: A review. *Environ. Pollut.* **2019**, *252*, 352–365. [CrossRef] [PubMed]
3. Katheresan, V.; Kansedo, J.; Lau, S.Y. Efficiency of various recent wastewater dye removal methods: A review. *J. Environ. Chem. Eng.* **2018**, *6*, 4676–4697. [CrossRef]
4. Pavithra, K.G.; Kumar, P.S.; Jaikumar, V.; Rajan, P.S. Removal of colorants from wastewater: A review on sources and treatment strategies. *J. Ind. Eng. Chem.* **2019**, *75*, 1–19. [CrossRef]
5. Daoud, M.; Benturki, O.; Girods, P.; Donnot, A.; Fontana, S. Adsorption ability of activated carbons from *Phoenix dactylifera* rachis and *Ziziphus jujube* stones for the removal of commercial dye and the treatment of dyestuff wastewater. *Microchem. J.* **2019**, *148*, 493–502. [CrossRef]
6. Sivalingam, S.; Sen, S. Efficient removal of textile dye using nanosized fly ash derived zeolite-x: Kinetics and process optimization study. *J. Taiwan Inst. Chem. Eng.* **2019**, *96*, 305–314. [CrossRef]
7. Li, J.; Li, H.; Yuan, Z.; Fang, J.; Chang, L.; Zhang, H.; Li, C. Role of sulfonation in lignin-based material for adsorption removal of cationic dyes. *Int. J. Biol. Macromol.* **2019**, *135*, 1171–1181. [CrossRef]
8. Chaari, I.; Fakhfakh, E.; Medhioub, M.; Jamoussi, F. Comparative study on adsorption of cationic and anionic dyes by smectite rich natural clays. *J. Mol. Struct.* **2019**, *1179*, 672–677. [CrossRef]

9.  Starukh, H.; Levytska, S. The simultaneous anionic and cationic dyes removal with Zn-Al layered double hydroxides. *Appl. Clay Sci.* **2019**, *180*, 105183. [CrossRef]

10.  Arora, C.; Soni, S.; Sahu, S.; Mittal, J.; Kumar, P.; Bajpai, P.K. Iron based metal organic framework for efficient removal of methylene blue dye from industrial waste. *J. Mol. Liq.* **2019**, *284*, 343–352. [CrossRef]

11.  Bhowmik, M.; Kanmani, M.; Debnath, A.; Saha, B. Sono-assisted rapid adsorption of anionic dye onto magnetic $CaFe_2O_4/MnFe_2O_4$ nanocomposite from aqua matrix. *Powder Technol.* **2019**, *354*, 496–504. [CrossRef]

12.  Zafar, M.N.; Dar, Q.; Nawaz, F.; Zafar, M.N.; Iqbal, M.; Nazar, M.F. Effective adsorptive removal of azo dyes over spherical ZnO nanoparticles. *J. Mater. Res. Technol.* **2019**, *8*, 713–725. [CrossRef]

13.  Tu, T.H.; Ngoc Cam, P.T.; Trong Huy, L.V.; Phong, M.T.; Nam, H.M.; Hieu, N.H. Synthesis and application of graphene oxide aerogel as an adsorbent for removal of dyes from water. *Mater. Lett.* **2019**, *238*, 134–137. [CrossRef]

14.  Jadhav, S.A.; Garud, H.B.; Patil, A.H.; Patil, G.D.; Patil, C.R.; Dongale, T.D.; Patil, P.S. Recent advancements in silica nanoparticles based technologies for removal of dyes from water. *Colloids Interface Sci. Commun.* **2019**, *30*, 100181. [CrossRef]

15.  Gouthaman, A.; Auslin Asir, J.; Gnanaprakasam, A.; Sivakumar, V.M.; Thirumarimurugan, M.; Riswan Ahamed, M.A.; Azarudeen, R.S. Enhanced dye removal using polymeric nanocomposite through incorporation of Ag doped ZnO nanoparticles: Synthesis and characterization. *J. Hazard. Mater.* **2019**, *373*, 493–503.

16.  Kubra, K.T.; Salman, M.S.; Hasan, M.N. Enhanced toxic dye removal from wastewater using biodegradable polymeric natural adsorbent. *J. Mol. Liq.* **2021**, *328*, 115468. [CrossRef]

17.  Ahamad, T.; Naushad, M.; Eldesoky, G.E.; Al-Saeedi, S.I.; Nafady, A.; Al-Kadhi, N.S.; Al-Muhtaseb, A.H.; Khan, A.A.; Khan, A. Effective and fast adsorptive removal of toxic cationic dye (MB) from aqueous medium using amino-functionalized magnetic multiwall carbon nanotubes. *J. Mol. Liq.* **2019**, *282*, 154–161. [CrossRef]

18.  Bagoti, N.; Sharma, A.K.; Kumar, S. A review on modified sugarcane bagasse biosorbent for removal of dyes. *Chemosphere* **2021**, *268*, 129309. [CrossRef]

19.  Da Silva, P.M.M.; Camparotto, N.G.; Neves, T.F.; Lira, C.T.G.; Mastelaro, V.R.; Picone, C.S.F.; Prediger, P. Effective removal of basic dye onto sustainable chitosan beads: Batch and fixed-bed column adsorption, beads stability and mechanism. *Sustain. Chem. Pharm.* **2020**, *18*, 100348. [CrossRef]

20.  Lin, T.-Y.; Chai, W.S.; Chen, S.-J.; Shih, J.-Y.; Koyande, A.K.; Liu, B.-L.; Chang, Y.-K. Removal of soluble microbial products and dyes using heavy metal wastes decorated on eggshell. *Chemosphere* **2020**, *270*, 128615. [CrossRef]

21.  Mijinyawa, A.H.; Mishra, A.; Durga, G. Cationic dye removal using a newer material fabricated by Taro Mucilage-g-PLA and Organobentonite clay. *Mater. Today Proc.* **2021**, *34*, 569–574. [CrossRef]

22.  Wazir, M.B.; Daud, M.; Ali, F.; Al-Harthi, M.A. Dendrimer assisted dye-removal: A critical review of adsorption and catalytic degradation for wastewater treatment. *J. Mol. Liq.* **2020**, *315*, 113775. [CrossRef]

23.  Al-Ahmed, Z.A.; Al-Radadi, N.S.; Ahmed, M.K.; Shoueir, K.; El-Kemary, M. Dye removal, antibacterial properties, and morphological behavior of hydroxyapatite doped with Pd ions. *Arab. J. Chem.* **2020**, *13*, 8626–8637. [CrossRef]

24.  Moosavi, S.; Lai, C.W.; Gan, S.; Zamiri, G.; Pivehzhani, O.A.; Johan, M.R. Application of Efficient Magnetic Particles and Activated Carbon for Dye Removal from Wastewater. *ACS Omega* **2020**, *5*, 20684–20697. [CrossRef]

25.  Amiralian, N.; Mustapic, M.; Hossain, M.S.A.; Wang, C.; Konarova, M.; Tang, J.; Na, J.; Khan, A.; Rowan, A. Magnetic nanocellulose: A potential material for removal of dye from water. *J. Hazard. Mater.* **2020**, *394*, 122571. [CrossRef] [PubMed]

26.  Wang, S.; Gao, H.; Fang, L.; Hu, Q.; Sun, G.; Chen, X.; Yu, C.; Tang, S.; Yu, X.; Zhao, X.; et al. Synthesis of novel $CQDs/CeO_2/SrFe_{12}O_{19}$ magnetic separation photocatalysts and synergic adsorption-photocatalytic degradation effect for methylene blue dye removal. *Chem. Eng. J. Adv.* **2021**, *6*, 100089. [CrossRef]

27.  Basaleh, A.A.; Al-Malack, M.H.; Saleh, T.A. Poly(acrylamide acrylic acid) grafted on steel slag as an efficient magnetic adsorbent for cationic and anionic dyes. *J. Environ. Chem. Eng.* **2021**, *9*, 105126. [CrossRef]

28.  Tătăruş, A.; Simonescu, C.M.; Scutariu, R.E.; Iancu, V.I.; Pirvu, F.; Puiu, D.; Galaon, T. HPLC detection of synthetic dyes in residual waters from wastewater treatment using adsorption on magnetic materials. *Rom. J. Ecol. Environ. Chem.* **2020**, *2*, 22–29.

29.  De Vargas Brião, G.; da Silva, M.G.C.; Adeodato Vieira, M.G. Neodymium recovery from aqueous solution through adsorption/desorption onto expanded vermiculite. *Appl. Clay Sci.* **2020**, *198*, 105825. [CrossRef]

30.  Langmuir, I. The adsorption of gases on plane surfaces of glass, mica and platinum. *J. Am. Chem. Soc.* **1918**, *40*, 1361–1403. [CrossRef]

31.  Freundlich, H.M.F. Über die adsorption in lösungen. *Z. Phys. Chem.* **1906**, *57*, 385–470. [CrossRef]

32.  Zhang, P.; Lo, I.; O'Connor, D.; Pehkonen, S.; Cheng, H.; Hou, D. High efficiency removal of methylene blue using SDS surface-modified $ZnFe_2O_4$ nanoparticles. *J. Colloid Interface Sci.* **2017**, *508*, 39–48. [CrossRef]

33.  Yousefi, T.; Yavarpour, S.; Mousavi, S.H.; Torab-Mostaedi, M.; Davarkhah, R.; Mobtaker, H.G. Effective removal of Ce(III) and Pb(II) by new hybrid nano-material: $H_nPMo_{12}O_{40}@Fe(III)_xSn(II)_ySn(I-)_{1-x-y}$. *Proc. Safe Env. Prot.* **2015**, *98*, 211–220. [CrossRef]

34.  Aliyan, N.; Mirkazemi, S.M.; Masoudpanah, S.M.; Akbari, S. The effect of post-calcination on cation distributions and magnetic properties of the coprecipitated $MgFe_2O_4$ nanoparticles. *Appl. Phys. A* **2017**, *123*, 446. [CrossRef]

35.  Briceño, S.; Suarez, J.; Gonzalez, G. Solvothermal synthesis of cobalt ferrite hollow spheres with chitosan. *Mater. Sci. Eng. C* **2017**, *78*, 842–846. [CrossRef]

36.  Fan, H.L.; Zhou, S.H.; Jiao, W.Z.; Qi, G.S.; Liu, Y.Z. Removal of heavy metal ions by magnetic chitosan nanoparticles prepared continuously via high-gravity reactive precipitation method. *Carbohydr. Polym.* **2017**, *174*, 1192–1200. [CrossRef]

37.  El-Shahawy, A.A.G.; Abo El-Ela, F.I.; Mohamed, N.A.; Eldine, Z.E.; El Rouby, W.M.A. Synthesis and evaluation of layered double hydroxide/doxycycline and cobalt ferrite/chitosan nanohybrid efficacy on gram positive and gram negative bacteria. *Mater. Sci. Eng. C* **2018**, *91*, 361–371. [CrossRef]

38.  Madian, N.G.; Mohamed, N. Enhancement of the dynamic mechanical properties of chitosan thin films by crosslinking with greenly synthesized silver nanoparticles. *J. Mater. Res. Technol.* **2020**, *9*, 12970–12975. [CrossRef]

39.  Pigorsch, E.; Elhaddao, A.; Turrell, S. Spectroscopic study of pH and solvent effects on the structure of Congo red and its binding mechanism to amyloid-like proteins. *Spectrochim. Acta* **1994**, *50A*, 2145–2152. [CrossRef]

40.  Kloster, G.A.; Mosiewicki, M.A.; Marcovich, N.E. Chitosan/iron oxide nanocomposite films: Effect of the composition and preparation methods on the adsorption of congo red. *Carbohydr. Polym.* **2019**, *221*, 186–194. [CrossRef] [PubMed]

41.  Zhu, H.; Zhang, M.; Liu, Y.; Zhang, L.; Han, R. Study of congo red adsorption onto chitosan coated magnetic iron oxide in batch mode. *Desalin. Water Treat.* **2012**, *37*, 46–54. [CrossRef]

42.  Kang, S.; Qin, L.; Zhao, Y.; Wang, W.; Zhang, T.; Yang, L.; Rao, F.; Song, S. Enhanced removal of methyl orange on exfoliated montmorillonite/chitosan gel in presence of methylene blue. *Chemosphere* **2020**, *238*, 124693. [CrossRef]

43.  Hu, P.; Zhang, L.; Huang, R.; Wang, J.; Liu, Q. Adsorption of methyl orange (MO) by Zr(IV)-immobilized cross-linked chitosan/bentonite composite. *Int. J. Biol. Macromol.* **2015**, *81*, 818–827.

44.  Culita, D.C.; Simonescu, C.M.; Patescu, R.E.; Preda, S.; Stanica, N.; Munteanu, C.; Oprea, O. Polyamine Functionalized Magnetite Nanoparticles as Novel Adsorbents for Cu(II) Removal from Aqueous Solutions. *J. Inorg. Organomet. Polym. Mater.* **2017**, *27*, 490–502. [CrossRef]

45.  Manjunath, S.V.; Kumar, M. Evaluation of single-component and multi-component adsorption of metronidazole, phosphate and nitrate on activated carbon from Prosopıs julıflora. *Chem. Eng. J.* **2018**, *346*, 525–534. [CrossRef]

46.  Mahamadi, C.; Nharingo, T. Competitive adsorption of $Pb^{2+}$, $Cd^{2+}$ and $Zn^{2+}$ ions onto Eichhornia crassipes in binary and ternary systems. *Bioresour. Technol.* **2010**, *101*, 859–864. [CrossRef]

47.  Wo, R.; Li, Q.-L.; Zhu, C.; Zhang, Y.; Qiao, G.-F.; Lei, K.-Y.; Du, P.; Jiang, W. Preparation and Characterization of Functionalized Metal–Organic Frameworks with Core/Shell Magnetic Particles ($Fe_3O_4@SiO_2@MOFs$) for Removal of Congo Red and Methylene Blue from Water Solution. *J. Chem. Eng. Data* **2019**, *64*, 2455–2463. [CrossRef]

48.  Zhou, H.-Y.; Fu, Y.-Q.; Jiang, R.; Jiang, J.-H.; Xiao, L.; Zeng, G.-M.; Zhao, S.-L.; Wang, Y. Adsorption removal of congo red onto magnetic cellulose/$Fe_3O_4$/activated carbon composite: Equilibrium, kinetic and thermodynamic studies. *Chem. Eng. J.* **2011**, *173*, 494–502. [CrossRef]

49.  Aoopngan, C.; Nonkumwong, J.; Phumying, S.; Promjantuek, W.; Maensiri, S.; Noisa, P.; Pinitsoontorn, S.; Ananta, S.; Srisombat, L. Amine-Functionalized and Hydroxyl-Functionalized Magnesium Ferrite Nanoparticles for Congo Red Adsorption. *ACS Appl. Nano Mater.* **2019**, *2*, 5329–5341. [CrossRef]

50.  Miao, J.; Zhao, X.; Zhang, Y.-X.; Liu, Z.-H. Feasible synthesis of hierarchical porous MgAl-borate LDHs functionalized $Fe_3O_4@SiO_2$ magnetic microspheres with excellent adsorption performance toward congo red and Cr(VI) pollutants. *J. Alloys Compd.* **2021**, *861*, 157974. [CrossRef]

51.  Liu, J.; Wang, N.; Zhang, H.; Baeyens, J. Adsorption of Congo red dye on $Fe_xCo_{3-x}O_4$ nanoparticles. *J. Environ. Manag.* **2019**, *238*, 473–483. [CrossRef]

52.  Barakat, M.A.; Kumar, R.; Lima, E.C.; Seliem, M.K. Facile synthesis of muscovite supported $Fe_3O_4$ nanoparticles as an adsorbent and heterogeneous catalyst for effective removal of methyl orange: Characterisation, modelling, and mechanism. *J. Taiwan Inst. Chem. Eng.* **2021**. [CrossRef]

53.  Zhang, Y.; Nan, Z. Preparation of magnetic $ZnLa_{0.02}Fe_{1.98}O_4$/MWCNTs composites and investigation on its adsorption of methyl orange from aqueous solution. *Mater. Res. Bull.* **2015**, *66*, 176–185. [CrossRef]

54.  Gao, L.; Zhang, Q.; Li, J.; Feng, R.; Xu, H.; Xue, C. Adsorption of Methyl Orange on Magnetically Separable Mesoporous Titania Nanocomposite. *Chin. J. Chem. Eng.* **2014**, *22*, 1168–1173. [CrossRef]

55.  Istraie, R.; Stoia, M.; Păcurariu, C.; Locovei, C. Single and simultaneous adsorption of methyl orange and phenol onto magnetic iron oxide/carbon nanocomposites. *Arab. J. Chem.* **2019**, *12*, 3704–3722. [CrossRef]

56.  Wu, D.; Zheng, P.; Chang, P.R.; Ma, X. Preparation and characterization of magnetic rectorite/iron oxide nanocomposites and its application for the removal of the dyes. *Chem. Eng. J.* **2011**, *174*, 489–494. [CrossRef]

57.  Zhu, H.Y.; Jiang, R.; Fu, Y.-Q.; Jiang, J.-H.; Xiao, L.; Zeng, G.-M. Preparation, characterization and dye adsorption properties of γ-$Fe_2O_3$/$SiO_2$/chitosan composite. *Appl. Surf. Sci.* **2011**, *254*, 1337–1344. [CrossRef]

58.  Hameed, B.H.; El-Khaiary, M.I. Malachite green adsorption by rattan sawdust: Isotherm, kinetic and mechanism modeling. *J. Hazard. Mater.* **2008**, *154*, 237–244. [CrossRef]

59.  Khan, T.A.; Dahiya, S.; Ali, I. Use of kaolinite as adsorbent: Equilibrium, dynamics and thermodynamic studies on the adsorption of Rhodamine B from aqueous solution. *Appl. Clay Sci.* **2012**, *69*, 58–66. [CrossRef]

60.  Mittal, H.; Al Alili, A.; Morajkar, P.P.; Alhassan, S.M. Graphene oxide crosslinked hydrogel nanocomposites of xanthan gum for the adsorption of crystal violet dye. *J. Mol. Liq.* **2021**, *323*, 115034. [CrossRef]